Journal Pre-proof

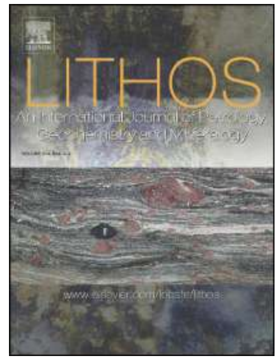

Late Paleozoic geodynamic evolution of the western North Patagonian Massif and its tectonic context along the southwestern Gondwana margin

Paulo Marcos, Cecilia Pavón Pivetta, Leonardo Benedini, Daniel A. Gregori, Mauro C. Geraldes, Nicolas Scivetti, Mercedes Barros, Maria E. Varela, Anderson Dos Santos

PII: S0024-4937(20)30438-2

DOI: https://doi.org/10.1016/j.lithos.2020.105801

Reference: LITHOS 105801

To appear in: *LITHOS*

Received date: 23 April 2020

Revised date: 15 September 2020

Accepted date: 22 September 2020

Please cite this article as: P. Marcos, C.P. Pivetta, L. Benedini, et al., Late Paleozoic geodynamic evolution of the western North Patagonian Massif and its tectonic context along the southwestern Gondwana margin, *LITHOS* (2020), https://doi.org/10.1016/j.lithos.2020.105801

Late Paleozoic geodynamic evolution of the western North Patagonian Massif and its tectonic context along the southwestern Gondwana margin

Paulo Marcos [a], Cecilia Pavón Pivetta [b], Leonardo Benedini [b], Daniel A., Gregori [b], Mauro C., Geraldes [c], Nicolas Scivetti [b] Mercedes Barros [b], Maria E., Varela [d], Anderson Dos Santos [c]

a. Instituto de Investigación en Paleobiología y Geología, UNRN-CONICET, Av. Julio A. Roca 1242, R 8332 EXZ, General Roca, Río Negro, Argentina.

b. Departamento de Geología, Universidad Nacional del Sur and INGEOSUR, San Juan 670, 8000 Bahía Blanca, Argentina.

c. Departamento de Geología Regional, Facultad de Geología, Universidad Estatal de Río de Janeiro, Rua São Francisco Xavier 534, Sala 3107F Maracanã, Brazil.

d. ICATE-CONICET, Av. España 1512 sur, 5400 San Juan, Argentina.

Abstract

In this study, we propose a geodynamic model covering sedimentation, metamorphism, magmatism, and exhumation processes for the western North Patagonian Massif basement. The youngest detrital zircon population ages (ca. 369 ± 8 Ma) obtained in a schist sample constrains the sedimentation stage to the Carboniferous Period. A first prograde metamorphic stage (M_1-D_1) produced the main foliation (S_1) under greenschist conditions (~ 500 °C, < 4.5 Kbars). This stage was possibly linked to the regional Carboniferous magmatism event (330 – 300 Ma). The Permian magmatism (ca. 290 Ma) likely induced partial melting and migmatization of the deepest metasedimentary suite. This event corresponds to the second prograde metamorphic stage (M_2) that reached amphibolite conditions (690 °C and 6.5 Kbars). The beginning of the basement uplift corresponds to the first retrograde metamorphic stage possibly developed during Permian – Triassic times (265 - 235 Ma). This event was triggered by NE-SW compression (σ_1) and developed folds (D_2-F_2), second foliation (S_2), micro-textural quartz deformation, and a retrograde evolution path for the garnet-bearing lithofacies. The final stage of the basement exhumation corresponds to the second retrograde metamorphic stage (D_3) developed by NNW-SSE compression and linked to open folds (F_3) in the Cushamen Formation. The characteristics of the western North Patagonian Massif geodynamic evolution and the adjacent basement regions suggest a paleotectonic subduction setting for the southwestern Gondwana margin during the late Paleozoic times.

Keywords: Geothermobarometry; Zircon U/Pb geochronology; Geodynamic evolution; Gondwana continent; Flat slab subduction; North Patagonian Massif.

1. Introduction

The different geothermobarometric conditions that the basement rocks experience during their evolutionary history is one of the most common objectives in studies of ancient igneous-metamorphic belts (Bucher and Grapes, 2008). The development of these evolutionary models commonly requires combined analyses, covering the petrological, structural, geochemical, and geochronological characterization of the orogen. In recent decades, several geodynamic models have been proposed to explain the evolution of the Paleozoic basement rocks located in the southwestern Gondwana continent (Forsythe, 1982; Ramos, 1984; Martín et al., 1999; Willner et al., 2004; Cawood, 2005; Pankhurst et al., 2006; Gregori et al., 2008; Rapalini et al., 2010; Martínez et al., 2012; Hervé et al., 2013, González et al., 2018; Oriolo et al., 2019; among others). However, the geodynamic evolution of some metamorphic igneous belts in this region of Gondwana remains to be understood.

The available studies of the late Paleozoic igneous-metamorphic rocks of the western North Patagonian Massif are a valuable source of information on the metamorphic, deformation, and magmatic processes involved in mountain building. However, these works lack careful geothermobarometric estimates, that are crucial to construct pressure-temperature diagrams. Moreover, a scarcity of geochronological analyses of metasedimentary units hampers a reconstruction of the whole tectonic-metamorphic history and its integration with the magmatic stages that affected the extra-Andean Patagonia region.

This contribution aims to present new geothermobarometric and geochronological data enabling to achieve a solid understanding of the evolution of the western North Patagonian Massif. This study was conducted in metamorphic and igneous rocks outcrops located near the Comallo locality, corresponding to the Cushamen and Mamil Choique formations (Fig. 1). Here we establish the petrographic, structural, geothermobarometric, and geochronological features of the metasedimentary rocks and propose a geodynamic model of sedimentation, metamorphism, magmatism, and exhumation for the western North Patagonian Massif basement during late Paleozoic times. Furthermore, we analyze and correlate each geodynamic evolution stage with neighboring regions in the attempt to understand the paleotectonic configuration of the southwestern Gondwana margin during that time.

2. Geological setting

In the Patagonia region, between 39° and 44° S, the metamorphic and igneous basement rocks crops out in the Lake Region (Chile), the Septentrional Patagonian Cordillera, the Neuquén Basin, the Extra-Andean Chubut, and the North Patagonian Massif (Argentina) (Fig. 1). The oldest recorded corresponds to metamorphic rocks of the Pampean Orogeny (Ediacaran-Cambrian) outcropping over the northeastern sectors of the North Patagonian Massif (Varela et al., 1997, 1998; Basei et al., 2002; González et al., 2002 y 2018; Pankhurst et al., 2006 and Greco et al., 2017). On the other hand, the igneous-metamorphic belts in the central North Patagonian Massif contain Cambrian - Ordovician granitoids (Rapalini et al., 2013 and Pankhurst et al., 2014) (Fig. 1).

In the western North Patagonian Massif, the Septentrional Patagonian Cordillera and the Lake Region (Chile), the U/Pb isotopic ages for the igneous basement units are younger than in the eastern and central sectors of the North Patagonian Massif (Varela et al., 2005; Pankhurst et al., 2006; Duhart et al., 2009, Hervé et al., 2013, 2016, 2018 and Serra-Varela et al., 2019). The oldest magmatic cycle for these regions has Silurian to Devonian ages (438 ± 2 - 361 ± 7 Ma), and its igneous bodies are emplaced into the metasedimentary rocks of Colohuincul Complex and equivalent units. The second and third magmatic events in the western Patagonia region developed during Carboniferous (330 ± 4 - 300 ± 2 Ma) and Permian (286 ± 13 Ma - 252 ± 2 Ma) times, respectively (Fig. 1; Varela et al., 2005, Pankhurst et al., 2006; Deckart et al., 2014; Gregori et al., 2020, among others). In the western North Patagonian massif, the igneous bodies of the Permian magmatism correspond to the Mamil Choique Formation and were emplaced into the metamorphic rocks of Cushamen Formation (González et al., 2003; Varela et al., 2005; von Gosen, 2009; Marcos et al., 2018; Gregori et al., 2020).

The evolutionary models proposed for the late Paleozoic basement of the western North Patagonian Massif indicate that the Cushamen Formation suffered several episodes of deformation, metamorphism, and magmatism. Dalla Salda et al., (1994) established three deformation events where the metamorphism reaches greenschist facies in the west and amphibolite conditions in the east in the outcrops of Río Chico. The metamorphic peak seems to be related to the Mamil Choique Formation magmatism, which produces the melting of the metasedimentary rocks (Volkheimer, 1973 and Dalla Salda et al., 1994). Later, Cerredo (1997), López de Lucchi et al., (2006) and Von Gosen (2009) recognize four deformation events in the Cushamen Formation. The first two are represented by S_1 and S_2 foliations, which were later folded during the last two deformation events (Table 6).

3. Analytical methods

3.1 Microprobe and whole-rock analyses

Three representative samples of different lithofacies were selected for chemical mineral and whole rock analyses. Major element chemical compositions were obtained with an ARL-SEMQ (WDS) electron microprobe at the ICATE, Argentina. Electron microprobe analyses were performed at 15 kV acceleration potential, giving 20 nA sample current and peak and background count times of 20 s and 10 s, respectively. Natural and synthetic standards were used for calibration, and an online ZAF correction was applied to the data. The microprobe data used for the geothermobarometric studies present a total range of: 100 ± 1.5 wt.% for garnet, 100 ± 1 wt.% for plagioclase, 96 ± 1.5 wt.% for biotite and 98 ± 1.2 for the muscovite. On the other hand, the whole-rock chemical composition was obtained by acid fusion using ICP-MS and ICP-ES at Bureau Veritas Laboratory (Canada). Procedure and geostandards can be consulted on the laboratory's webpage.

3.2 U/Pb zircon dating

U/Pb detrital zircon datings of schist sample (PC44D) were performed at the Laboratory of geochronology and radiogenic isotopes (MultiLab) at the Rio de Janeiro State University (UERJ), employing the in situ LA-MC-ICPMS procedures (Geraldes et al. 2015 and Costa et al. 2017). After obtaining cathodoluminescence images with a scanning electron microscope (SEM-Quanta 250), in situ analyses were performed using a Teledyne Analyte G2 Excimer Laser Ablation System coupled to a Thermo Scientific Neptune Plus MC-ICP-MS. The procedure of each measurement cycle consisted of the following steps: blank; GJ-1 standard; nine zircon spots samples; 91500 standard; GJ-1 standard; blank. The primary (GJ-1) and secondary (91500 - Fig. A and Table A in supplementary data) standards allow us to estimate the necessary corrections and evaluate the isotope ratios and inter-element fractionation data. The blank values were obtained in the same conditions as the standard and zircon spots samples. The detrital zircon ages were calculated using ISOPLOT 4.15 (Ludwig, 2003).

4. Field relationships and structure

The schists of the Cushamen Formation form sequences with two main foliation (S_1) orientations along the railroad track (N 330°/30° SW - N 20°/30° NW) and National Route N° 23 (N 315°/40° SW - N 25°/45° NW) (Figs. 2 and 3a). Both orientations develop symmetrical open folds (F_3) with wavelength of a hundred meters, a 253°/28° fold axes plunging direction, and axial planes dipping 75°- 85° to the southeast (Fig. 2). In addition, the schists preserve asymmetrical, isoclinals, and open folds (F_2) with centimetric and micro-scale wavelength, fold axes with an average plunging direction of 141°/25°, and axial planes dipping 35°- 45° to the southwest (Figs. 2, 3e, 4b and 4c).

The migmatites are widely distributed in the Comallo creek area and locally in the contact between the Mamil Choique and Cushamen formations in the other regions of the study area. In the Comallo creek area, the migmatites display a centimetric compositional banding oriented N 30°/30° NW and in some outcrops develop disharmonic fold with NW-SE fold axes direction (~150°), linked to the F_2 (Figs. 2, 3c and 3d). On the other hand, the granodioritic igneous outcrops of the Mamil Choique Formation have an N 310°/60° SW foliation orientation (Figs. 2 and 3b). Both metamorphic and igneous units are emplaced by dikes of the Neneo Ruca Formation (Fig. 2 and 3a).

5. Lithofacies

5.1 Mica-schists

The mica-schists lithofacies are distributed sparsely in comparison with other lithofacies and are characterized by an alternation of microlithons with lepidoblastic and granoblastic textures (Fig. 4a). These lithofacies are composed of muscovite (40-45%), quartz (25-35%), biotite (20-25%), and plagioclase (3%). Chlorite is present in limited quantities along the boundary of the biotite, and sericite was recognized inside twin planes of plagioclases and muscovite. However, in some samples, the chlorite could be present in proportions of ~ 5% and without a clear relationship to the biotite. Apatite, rutile, zircon, and opaque minerals are present in minor quantities.

The biotite and muscovite develop lepidoblastic texture and define the main foliation (S_1). Moreover, it is possible to recognize microfolds (F_2), where the second generation of muscovite (S_2) develops its axial planes with an angle of ~ 30° with respect to the main foliation (S_1) (Figs. 4b and 4c). Quartz appears in two textural types. The polycrystalline aggregates develop ribbon quartz following the main foliation (S_1) and some display microfolds (F_2) (Figs. 4a and 4c). On the other hand, isolated quartz grains are very scarce. Both textural types show the development of subgrains linked to dislocations oriented perpendicular to the boundary grains. The plagioclases are subidioblastic and usually show partially homogenized polysynthetic twins. The boundary between plagioclases and quartz are generally lobate and sometimes serrate.

According to textural and mineralogical features, it is possible to distinguish three mineral associations (Table 1). The mineral association A (MAA), is composed of Qz + Ms + Bt + Pl ± Chl and defines the main foliation (S_1). The mineral association D (MAD), is linked to the second foliation and is composed of Ms + Qz. The third mineral association F (MAF), corresponds to the chlorite and sericite (Chl + Src).

5.2 Quartz-mica schists

The most representative lithofacies in the study area are the quartz-mica schists. These rocks have lepidogranoblastic or granolepidoblastic textures and are constituted by quartz (35-40%), biotite (30-40%), plagioclase (10-25%), and muscovite (1-5%). There are minor quantities of chlorite, zircon, apatite, and opaque minerals. Titanite and epidotes were recorded only in some samples.

As in mica-schist lithofacies, the main foliation (S_1) is mainly defined by biotite and muscovite. The second generation of muscovite and biotite (S_2) was also identified. Most isolated quartz crystals show twistwall (perpendicular) and tiltwall (parallel) dislocations, following the classification of Passchier and Trouw (2005) (Fig. 4e). Furthermore, neoformed quartz and the polycrystalline aggregates were distinguished in thin sections (Fig. 4e). The plagioclase is parallel to the main foliation and show variable degrees of homogenization, from polysynthetic twins perfectly preserved and sometimes curved, to completely homogenized grains.

The textural and mineralogical characteristics of these lithofacies allow us to distinguish three mineral associations (MAA-MAE-MAF) similar to those of the mica-schist lithofacies. However, in the quartz-mica schist lithofacies, the second mineralogical association (MAE) that defines the second foliation (S_2), includes biotite in addition to muscovite and quartz (Table 1).

5.3 Quartz-mica-garnet schists

The quartz-mica-garnet schists are distributed locally near to the contact with the intrusive bodies or adjacent to the migmatites. These lithofacies commonly have porphyrolepidoblastic or granolepidoblastic textures and are constituted by quartz (35-40%), biotite (25-30%), plagioclase (10-25%), muscovite (5%) and garnet (~ 1 - 2 %). In some samples, chlorite and sericite are at the boundaries with biotite and muscovite, respectively. Opaque minerals, titanite, and zircons appear as accessory minerals.

Quartz grains are commonly distributed in polycrystalline aggregates that form discontinuous ribbons following the main foliation. In such contexts, quartz exhibits wavy extinction and dislocations of the twistwall subtype. Biotite and muscovite develop the main foliation (S_1), and also display the secondary foliation (S_2) with identical characteristics in the other schist lithofacies (Fig. 4d). Plagioclase and garnets appear mainly as isolated porphyroblasts between the quartz and biotite-muscovite microbands. Only a few garnets have fractures and inclusions of zircons, biotite, and plagioclase.

There are three mineral associations in the quartz-mica-garnet schist lithofacies (Table 1). The MAA corresponds to the association that defines the main foliation (S_1), whereas the MAB is composed of Qz + Ms + Bt + Pl + Grt, which differs from the MAA by the presence of garnets in contact with the minerals that define the main foliation. The last mineral association corresponds to the MAF (Table 1).

5.4 Stromatic metatexites

Stromatic metatexites have leucosome layers oriented parallel to the main foliation of the schists that form the paleosome (Fig. 3c). In some outcrops, it is possible to recognize that the melt supply comes from dikes that cut the schists. Therefore, at least part of the melt in those areas was injected from dikes and allows us to classify the leucosomes as a leucogranitic veins subtype (Sawyer, 2008). On the other hand, were recognized thin biotite-rich bands corresponding to the melanosome. This part of the stromatic migmatites is located inside the leucosome bands and near the boundaries between the paleosome and leucosome (Fig. 3d).

In the metatexites, the leucosome has a fine-grained and equigranular texture and is mainly composed of quartz (30-45%), feldspars (microcline ~ 20% and plagioclase ~ 30%) and lesser quantities of muscovite (1-3%), biotite (2%) and garnet (2%). Scattered zircons and sillimanites are observed inside the feldspars. Quartz grains have wavy extinction, twistwall-tiltwall subgrains with lobate grain boundaries and chessboard intracrystalline textures. The plagioclase shows partially homogenized twins while the microcline commonly presents twin boundary migration. Contact boundaries between feldspars and quartz have myrmekite texture in some samples.

The paleosome has a granolepidoblastic or porphyroblastic texture (Fig. 4g), and is composed of quartz (40%), biotite (20-35%), a variable plagioclase content (0-25%), garnet (from 2-15%, although it can reach 30%) and muscovite (5-25%). There are minor quantities of zircon, opaque minerals, apatite, and in some samples, sillimanite. Biotite and muscovite usually develop a lepidoblastic texture that defines the main foliation (S_1), and show alteration to chlorite and sericite, respectively. Quartz has lobate to serrate boundaries and subgrain domains with tiltwall or chessboard subtype textures (Fig. 4f). The plagioclase is oriented parallel to the main foliation and in some cases preserved the polysynthetic twins. Garnets are subidioblastic, and some of them are fractured and contain inclusions of quartz and biotite.

The MAA is the oldest mineral association preserved in the paleosome (Table 1). On the other hand, mineral associations B and C (MAB-MAC) are represented by the presence of garnet, and in some samples sillimanite. The last mineral association differentiated on the paleosome corresponds to the MAF (Table 1).

6. Mineral Chemistry

6.1 Mica-schist and quartz-mica schist

The mica-schist and quartz-mica schist lithofacies were analyzed by means of sample P35, extracted from the western outcrop of the railroad track. The biotites that integrate the main foliation have Si contents between 2.63 and 2.77 atoms per formula unit (a.p.f.u.) (Table 2). In accordance with the values of the #Mg (0.42- 0.47) and Al (VI) (0.27-0.42) contents, the biotite is classified in the field of the annites in the annite-phlogopite-siderophyllite-eastonite diagram. The white micas show Si content between 3.01 and 3.07 a.p.f.u., low Na content (0.05 a.p.f.u.), and nil Ca (Table 2). The values lower than 3.1 for Si and the limited Na and Ca content, allow us to classify these white mica as muscovite (Rieder et al., 1998 and Guidotti, 1984). On the other hand, most plagioclases are not zoned and have an average X_{Ab} of 0.66. In those that are zoned, the core and rim have X_{Ab} of 0.65 and 0.69, respectively (Table 2).

6.2 Quartz-mica-garnet schist

Sample P49, corresponding to the quartz-mica-garnet schist lithofacies, was selected from eastern outcrops along National Route N° 23. This sample contains weakly zoned almandine garnets due to variations in the content of CaO, MgO, MnO (Table 2 and Fig. B in supplementary data). The garnet cores have 3.9 ± 0.3 mol % of grossular, 11.2 ± 0.4 mol % of pyrope, 76.1 ± 0.7 mol % of almandine and 8.85 ± 0.6 mol % of spessartine. The rim composition of these garnets presents greater dispersion than the cores and has 5.1 ± 1.2 mol % of grossular, 8.7 ± 1.9 mol % of pyrope, 76.1 ± 1 mol % of almandine and 10.2 ± 1.6 mol % of spessartine.

The biotites that integrate the main foliation have between 2.58 and 2.73 a.p.f.u. of Si. The included biotites in garnets have a similar Si content and are a little lower in MgO than the foliated biotites (Table 2). The #Mg variations for both types of biotite are between 0.41 and 0.43, while the Al (VI) content average is 0.31-0.36 a.p.f.u. The relationship between #Mg and Al (VI) corresponds to annite. The Si content in the white micas varies between 3.05 and 3.07 a.p.f.u. and ~ 0.08 a.p.f.u. of Na (Table 2). These values, similar to those obtained in sample P35, allow us to classify these micas as muscovite. The analyses in zoned plagioclase show core and rim with X_{Ab} of 0.68 and 0.76, respectively (Table 2).

6.3 Stromatic migmatite

The paleosome of sample P7 was extracted from the eastern railroad track outcrops. This sample contains almandine garnets with variations in MgO and MnO content (Table 2 and Fig. B in supplementary data). The cores have an average composition of 3.6 ± 0.15 mol % of grossular, 13.55 ± 0.7 mol % of pyrope, 75.15 ± 0.52 mol % of almandine and 7.7 ± 0.3 mol% of spessartine. The rims of these garnets are compositionally defined by a 3.6 ± 0.16 mol % of grossular, 11.9 ± 0.47 mol % of pyrope, 76.2 ± 0.55 mol % of almandine and 8.31 ± 0.5 mol % of spessartine.

The biotites that integrate the main foliation of the paleosome have between 2.58 and 2.73 a.p.f.u. of Si. The included biotites in the garnet have similar contents, although they are less rich in Mg (Table 2). The #Mg variations for foliated and included biotite are between 0.40 and 0.36 and the Al (VI) average content is 0.35 – 0.37 a.p.f.u, respectively. As in the samples of the other lithofacies, the relationships of #Mg and aluminum (VI) correspond to annite. The Si content of the white micas varies from 3.06- 3.09 a.p.f.u. and in Na ~ 0.08 a.p.f.u. (Table 2). These results, which are similar to the white micas from the schists lithofacies, allow them to be classified as muscovite. The plagioclases are zoned with an average composition of X_{Ab} 0.71 in the core to X_{Ab} of 0.75 in the rim (Table 2).

7. Thermobarometry

The petrography and microprobe data were used to determine the geothermobarometric parameters using the Excel spreadsheet GPT (Reche and Martínez, 1996), TWQ (Berman, 1991), and Perple_X (Conolly, 1990) software. The pressure and temperature ranges selected for all diagrams lie from 1-10 Kbars and 450-800°C.

7.1 Conventional geothermobarometry

The mineral associations and mineral chemistry results allow us to establish a set of possible reactions and to estimate the pressure and temperature conditions by means of thermodynamic calibrations (Table 4). Taking into account the compositional variations in garnet and plagioclase, these changes were used to define core and rim thermodynamic conditions in garnet-bearing lithofacies (P49 and P7). In these two lithofacies, we combined the core-compositions with the average chemical composition of included biotite and, for the rim, the analyses of foliated biotite in contact with garnets and plagioclase (Table 2). For the mica-schist and quartz-mica schist lithofacies, we used all the chemical variations of the micas obtained in sample P35.

The mineral association A (MAA - Table 1) of the quartz-mica schists (P35), was evaluated with the Mg-Tschermak exchange geothermometer reaction between muscovite and biotite (R1-Table 4). The average result obtained for this reaction in the GPT spreadsheet was 517 °C (Table 5). On the other hand, the mineralogical association Qz + Ms + Bt + Pl + Grt (MAB - Table 1), corresponding to the quartz-mica-garnet schist (P49), makes it possible to estimate temperature and pressure with the R2 and R3 reactions (Table 4). The combination of plagioclase and garnet core composition gives 629 °C and 4.14 Kbars using the GPT spreadsheet and 593 °C and 3.64 Kbars with the TWQ (Fig. 5a - Table 5). Moreover, we obtained 559 °C and 4.19 Kbars using the GPT spreadsheet and 556 °C - 3.61 Kbars in TWQ for plagioclase and garnet rims composition (Fig. 5a - Table 5).

The mineral association B and C of the stromatic migmatites (P7) was evaluated using the geothermometer Grt-Bt (R2) and the geobarometers GBP (R3), GASP (R4), and GBSQ (R5) (Table 1 and 4). For plagioclase and garnet core compositions, the temperature obtained using the geothermometer Grt-Bt in the GPT spreadsheet was 698 °C. The GBP and GASP geobarometer results were on average 5.45 and 5.77 Kbars, respectively (Table5). With the TWQ, the result of the temperature and pressure reaction intersection was: (a) The R2-R3 intersection occurs at 698 °C and 5.59 Kbars (Fig. 5b), (b) The R2-R4 intersection at 697 °C and 5.4 Kbars (Fig. 5c) and (c) The R2-R5 intersection at 702 °C and 6.37 Kbars (Fig. 5d). Moreover, we obtained a temperature of 649 °C (R2) and a range of pressures between 4.49 Kbars (R3) and 4.97 Kbars (R4) for the plagioclase and garnet rim compositions in the GPT spreadsheet (Table 5). The intersection of reactions in TWQ indicates the following average values for the rim compositions: (a) 651 °C and 5.42 Kbars for R2-R3 (Fig. 5b), (b) 653 °C and 5.34 Kbars for R2-R4 (Fig. 5c), and (c) 651 °C and 5.55 Kbars for the last pair of reactions (R2-R5 - Fig. 5d).

7.2 P-T pseudosections models

The P-T pseudosections were modeled using the Perple_X software package (Conolly, 1999. The August 2006 version was downloaded from http://www.perplex.ethz.ch). We used an internally consistent thermodynamic data set of Holland and Powell (1998) for minerals and the equations of Holland and

Powell (1991, CORK model) for H_2O. In addition, we used the following solid solution models compatible with this data set: Chl (HP) for chlorite, TiBio (HP) for biotite, Ep (HP) for epidote-zoisite, Pheng (HP) for white micas, hCrd for cordierite, Amph (DHP) for amphibole, Gt (HP) for garnet, fsp11 and fsp21 for plagioclase and K-feldspar in accordance with Fuhrman and Lindsley (1988). St (HP) was used for staurolite, Cpx (HP) for clinopyroxene, Opx (HP) for orthopyroxene, and melt (HP) for the melted part. We used the subprograms werami.exe and pscontor.exe of the Perple_X software to obtain isopleths for molar fractions of garnet and white mica components as well as the modal proportions of garnet.

The whole-rock results of the pseudosection were simplified to an eleven component system: SiO_2, Al_2O_3, FeO, MgO, CaO, MnO, Na_2O, K_2O, TiO_2, H_2O, O_2 (MnNCKFMASHTO, Table 3). The O_2 content was estimated at 5% of the Fe^{+3}/Fe^{+2} ratio (e.g., Massonne et al., 2012 and Martínez et al., 2017), and the P_2O_5 content was removed as well as a reduction of CaO, given that both oxides derive from apatite. The schist samples were modeled with 2.6% of H_2O, while we used 2.0% of H_2O for the migmatite P-T pseudosection (Table 3). The water content estimate ranges between 2% and 4% for schists with biotite and garnet, and around 2% for migmatites, as proposed by Bucher and Grapes (2008).

7.2.1 Quartz-mica schist

In the P-T pseudosection of the quartz-mica schists (sample P35), quartz and plagioclase are stable over the entire P-T range (Fig. 6a). Biotite is stable neither at high temperatures - low pressures nor at low temperatures - high pressure fields. Muscovite forms mineral associations at moderate to low temperatures, and displays a positive stability curve from 555 - 755 °C. At temperatures lower than 550 °C, the mineral association fields include chlorite and epidote. The garnet stability curve presents an irregular negative slope between 1 Kbar - 755 °C and 6.4 Kbars - 450 °C. The K-feldspar is stable only at pressures below 3 Kbars, and temperatures between 550 °C and 750 °C. The melting curve at pressures lower than 3.7 Kbars presents a negative trend between 750 and 670 °C, whereas above this pressure a high P/T gradient develops, ending at 665 °C and 10 Kbars.

The mineral association Qz + Ms + Bt + Pl ± Chl (MAA- table 1) of the quartz-mica schists is stable at pressures of between 1 and 5.5 Kbars and temperatures of 450-600 °C in the modeled P-T pseudosection (Fig. 6a). In addition, a comparison between the modeled Si muscovite isopleths against microprobe data (3.01 - 3.07 a.p.f.u) allows us to consider the pressure range of stability to lower than 4.5 Kbars for the quartz-mica schists lithofacies.

7.2.2 Quartz-mica-garnet schist

The P-T pseudosection of the quartz-mica-garnet schist (P49) (Fig. 7), shows a similar design to that of the quartz-mica schist (P35). Plagioclase and quartz are stable in the whole range of temperatures and pressures, except at very high temperatures and low pressure for quartz (Fig. 7a). The partial melting curve and the curves that define the stability fields for biotite, chlorite, muscovite, and K-feldspar are very similar to those of the quartz-mica schist. One of the differences between the P-T pseudosection models of sample P35 and sample P49 is the Al_2SiO_5 polymorphs occurrence in the latter.

In the P-T pseudosection, the modeled grossular content (X_{Ca}) grows from 3 to 30 mol % as pressure increases and temperature decreases. By contrast, the pyrope content (X_{Mg}) increases from 1 mol % at 450 °C to 25 mol % at 800 °C (Fig. 7b). The linkage between microprobe data and these isopleths for garnet core and rim compositions falls into the stability field of Ms-Pl-Bt-Grt-Qz-Opq mineral association (MAB - table 1 and Figs. 7a and 7b). Taking into account the grossular and pyrope molar fractions, the average temperature and pressure estimated for the garnet core crystallization in this P-T pseudosection were 658 °C and 5.5 Kbars, whereas the rim composition recorded an average temperature of 601 °C and 4.9 Kbars (Fig. 7b and Table 5). Moreover, the pressure and temperature estimates for core and rim garnet compositions fall into the low garnet content (~1 %) range and in the range 3.06 – 3.08 Si a.p.f.u of muscovite (Fig. 7b). Both mineral variables are compatible with the microprobe data and petrographic observations (Table 2 – Fig. 7b).

7.2.3 Stromatic migmatite

In the paleosome P-T diagram of the stromatic migmatites (P7), garnet, quartz, and biotite are stable in the entire P-T range, except over a limited field at high temperatures and low pressures where quartz is unstable (Fig. 8a). Only at temperatures above 730 °C and high pressures is plagioclase unstable. Muscovite occurs at moderate to lower temperatures, while K-feldspar at moderate to high temperatures. The partial melting curve has a negative slope that starts at 755 °C - 1 Kbar and ends at 635°C - 10 Kbars. This curve has a relatively constant temperature of ~ 660 °C between 3.3 and 7.3 Kbars.

In the P-T pseudosection, the grossular content (X_{Ca}) varies from 3 - 8 mole %, increasing from low pressures and moderate temperatures to high pressures and low temperatures. By contrast, the molar proportions of pyrope (X_{Mg}) vary between 6 and 30 %, increasing from low pressures and temperatures to high pressure and temperatures (Fig. 8b). The linkage between the microprobe data (Table 2) and these isopleths indicates that the crystallization conditions for the garnet core were stable with the Ms-Pl-Bt-Grt-Sil-Qz-Opq-Liq field, and reach an average temperature of 690 °C and 6.7 Kbars of pressure. The core plots on the melting field are possibly linked to the incorporation of a small neosome fraction of the migmatites lithofacies in the modeled sample (P7). On the other hand, the rim microprobe compositional data fall within the Ms-Pl-Bt-Grt-Sil-Qz-Opq field and the P-T average estimations reach 6 Kbars and 655 °C (Fig. 8b - Table 5). The totality of the compositional garnet variations represent the third mineral association of the migmatite lithofacies (MAC-Table 1) and fall into the range of 12-15 % garnet modal proportion, comparable with the petrographic observations (Fig. 4g). In addition, the Si muscovite contents for the garnet plots in the modeled P-T pseudosection (3.06 - 3.09 a.p.f.u) are compatible with the microprobe data (Table 2).

8. U/Pb detrital zircon ages

Sample PC44D was selected from the western railroad track outcrops for detrital zircon age analysis. This sample corresponds to the mica-quartz schist lithofacies of the Cushamen Formation and contains unfractured zircon crystals of medium size (90 - 225 μm). Most of these minerals have a prismatic shape with a subhedral and subrounded boundary (Fig. 9a). Only a few specimens have an ovoid shape and anhedral – rounded crystal edges.

A total of 94 zircon grains from 135 dated samples have a percentage of concordance equal to or better than 90 % (Fig. 9b and Table C in supplementary data). The U/Pb analyses yield ages from Precambrian to Carboniferous that can be differentiated into five detrital zircon populations (Fig. 9c). The Neoarchean – Paleoproterozoic zircons aged from 2300 to 2600 Ma are scarce and represent the oldest records (P1 – Fig. 9). On the other hand, the second population, P2, is the biggest and includes most of the Mesoproterozoic – Neoproterozoic zircons (P2 – Fig. 9). Population P3 consists of Cambrian and Neoproterozoic zircons with the main peak at ca. 525 Ma (Fig. 9c). The Ordovician population (P4) is the most abundant Paleozoic detrital zircon provenance and has its main peak at ca. 474 Ma (Fig. 9c). The youngest population (P5) contains Silurian to Carboniferous zircons and has two main peaks at 438 Ma and 369 Ma. The last peak is considered the maximum depositional age for the Cushamen Formation in the outcrops near Comallo.

9. Discussion

9.1 Geodynamic evolution stages of the western North Patagonian basement

The analysis of the western North Patagonian basement defines three main evolutionary stages related to sedimentation, prograde and retrograde metamorphism (Fig. 10). In addition, the petrographic, thermobarometry and structural results allow us to differentiated two events for each metamorphic stage.

9.1.1 Sedimentation stage

The sedimentation age of the Cushamen Formation protolith has been the subject of several studies which provided contrasting results. According to Cerredo and López de Luchi, (1998) sedimentation took place during pre-Carboniferous times, while Duhart et al., (2002), Hervé et al., (2005) and Marcos et al., (2018) suggest formation in the Carboniferous. Based on the U/Pb ages presented here on the Cushamen Formation, the younger population of detrital zircons points to an age of sedimentation younger than 369 ± 8 Ma (Figs. 9 and 10), i.e. probably later than Upper Devonian.

The Precambrian detrital zircon populations (P1 and P2) are an important provenance source (Fig. 9c) possibly comes from the ancient western Gondwana massifs (e.g., the Rio de La Plata Craton). Cambrian and Ordovician zircons (P3 and P4 - Fig. 9c) are probably related to the magmatism and metamorphism recorded in the eastern North Patagonian Massif, while the Silurian-Devonian population (P5 - Fig. 9c) possibly comes from igneous units that are presently in the Lake Region (Chile), the Septentrional Patagonian Cordillera and the North Patagonian Massif (Marcos et al., 2018).

9.1.2 Prograde metamorphism

9.1.2.1 First prograde metamorphic stage

In the study area, the first tectonic-metamorphic event (M_1-D_1) is defined by the Qz-Ms-Bt-Pl mineral association of the main foliation (S_1), preserved in the schists and in most the migmatites (MAA - Table 1). This foliation is the oldest registered in the study area and is comparable to the main foliation in areas close to Comallo (González et al., 2003; Von Gosen, 2009), in turn, correlated with the D_2-S_2 foliation of the Cushamen Formation near Río Chico (Cerredo and López de Luch, 1998).

Based on the syn-tectonic mineral assemblage, we conclude that the first tectonic-metamorphic stage developed under greenschist facies conditions. A similar interpretation was given by Cerredo and López de Luchi, (1998) and Von Gosen, (2009). For this event, geothermobarometry results of quartz-mica schists (Table 5), indicates temperature and pressure conditions close to 500 °C and 1 – 4.5 Kbars corresponding to upper crust levels (Bucher and Grapes, 2008).

This first prograde metamorphic stage (M_1-D_1) must have occurred between the maximum age of sedimentation of ca. 369 ± 8 Ma presented here and the oldest records of the Permian magmatism in the studied area ~290 Ma (Varela et al., 2005 and Gregori et al., 2020) (Fig. 10). The Carboniferous tectonic-magmatic event recorded between 330 to 300 Ma in the southwestern region of Gondwana might have triggered this early event (Fig.1 - Pankhurst et al., 2006 and Deckart et al., 2014). A correlative period (335-300 Ma) for the main foliation development in the Cushamen Formation outcrops near Río Chico was suggested by Lopez de Luchi et al. (2006) (Table 6).

9.1.2.2 Second prograde metamorphic stage

The quartz-mica-garnet schist and stromatic migmatites are located near the Permian igneous outcrops of the Mamil Choique Formation. These metamorphic lithofacies contain garnet, indicating a higher metamorphic grade than the mica and quartz-mica schists. Besides the garnet development, the other mineral and textural change linked to the second prograde metamorphic stage (M_2) is the enlargement of the main foliation micas (S_1). On the other hand, the thermobarometric results indicate that the garnet-bearing lithofacies recorded an increment of ~ 200 °C and 1.5 - 2 Kbars with respect to the mica and quartz-mica schist lithofacies (Table 5). In addition to the thermal input linked to the Permian magmatism, the pressure differences probably show that magmatism and partial melting process developed in the deepest conditions of the schists' sequence (Fig.

10). Both pressure and temperature results indicate that the garnet-bearing lithofacies development achieved the upper greenschist and amphibolite metamorphic facies during this event, recording the highest P-T conditions in the studied area.

The changes produced in the Cushamen Formation by the Permian magmatism were previously recognized in the studied area by Volkheimer (1973) and Von Gosen (2009), who associated the granodiorite and tonalite facies of the Mamil Choique Formation to migmatite development. Similar relationships between magmatism and metamorphism were also established by other authors near Río Chico and Mamil Choique (Table 6) (Dalla Salda et al., 1994; Cerredo and López de Luchi, 1998). Permian magmatism started ca. 290 Ma in the outcrops near the Comallo area (Varela et al., 2005; Pankhurst et al., 2006 and Gregori et al., 2020). Therefore, we considered the oldest records for the Permian magmatism (~ 290 Ma) as the probable age for the last stage of the prograde metamorphic evolution (M_2) (Fig. 10).

9.1.3 Retrograde metamorphism

9.1.3.1 First retrograde metamorphic stage

The first retrograde metamorphic stage is linked to the second deformation event (D_2 - F_2), which is recognizable in the schist and the migmatites of the Cushamen Formation as well as in the igneous bodies of the Mamil Choique Formation (Figs. 2, 3b, 3d and 3e). Taking into account the F_2 folds features and the Mamil Choique foliation orientation, it is possible to suggest a NE-SW (~220°) compression direction for the second deformation stage, and in turns correlate this stage with the D_3 deformation of Von Gosen (2009) (Fig. 10 and Table 6).

Furthermore, the main textural and mineralogical attributes of the second deformation stage (D_2) include: (a) S_2 axial plane foliation formed by muscovite, biotite and quartz in the schist lithofacies (MAD and MAE - Table 1; Figs. 4b and 4d), (b) Microfolds (F_2) of the S_1 foliations (Figs. 4b and 4c), (c) Quartz and plagioclase intracrystalline deformation and quartz neoformation in grains boundaries (Figs. 4e and 4f) and (d) P-T changes associated with the core and rim garnet compositions. The thermobarometry results for garnet-bearing lithofacies show that the garnet rims record lower P-T conditions than the cores (Fig. 11 and Table 5). This behavior is probably related to the second deformation stage (D_2), which triggered the decrease in pressure and temperature conditions after the last prograde metamorphic stage (M_2). Following the Passchier and Trouw (2005) temperature estimates, the chessboard texture distinguished in the migmatites lithofacies was possibly developed from 500 - 700°C. This range fits with the falling of temperature records for the core to rim garnet composition results (Table 5). On the other hand, neoformation of quartz with lobate and serrate intercristalline contacts is usually found in the mica and quartz-mica schist lithofacies and possibly developed from 400 - 500 °C (Hirth and Tullis, 1992 and Passchier and Trouw, 2005). This last temperature estimate could be correlatable with greenschist grade for the MAD and MAE (Table 1) developed in the mica and quartz-mica schist lithofacies during the first retrograde stage (D_2 - S_2).

In summary, the characteristics of the first retrograde metamorphic stage allow us to suggest that this event (D_2) was developed under greenschist facies (S_2) and triggered the basement exhumation beginning (Figs. 10 and 11). Varela et al., (1999 and 2005) and Lopez de Luchi et al., (2006) conducted K/Ar dating in several granites and schists in the western North Patagonian Massif, obtaining ages of between 235 ± 8 Ma and 265 ± 6 Ma. These ages may represent the time of the first retrograde metamorphic stage and the thermal decline of the igneous - metamorphic basement (Fig. 10).

9.1.3.2 Second retrograde metamorphic stage

The features of the F_3 open folds related to the last deformation event allow us to suggest an NNW-SSE (~345°) principal stress (σ_1) direction for the third deformation stage (D_3) (Fig. 10). The mineral and textural changes of this second retrograde metamorphic stage are possibly linked to the biotite and muscovite retrogression to chlorite and sericite, respectively (MAF-Table 1). We associate this last event with the final uplift stage of the basement in the western North Patagonian Massif which might be correlated with the deformation stage D_4 proposed by Cerredo and López de Luchi, (1998) in the Rio Chico area (Table 6).

9.2 Geodynamic evolution of the southwestern Gondwana basements

The oldest late Paleozoic records are linked to the sedimentation of the Cushamen Formation developed in the western North Patagonian basin (Fig. 10 and 12a). These records are contemporaneous with some of the sedimentary and metasedimentary sequences of the Extra-Andean Chubut, Septentrional Patagonian Cordillera and Lake Region. The paleogeographic configuration shows that these regions developed a connected basin, while the North Patagonian basin was more extensively developed inside the Gondwana continent and partially disconnected by the Silurian - Devonian topographic high (Fig. 12a – Marcos et al., 2018 and Suárez et al., 2019).

During the late Carboniferous tectonic-magmatic stage (330-300 Ma), the basements of the Lake Region and Septentrional Patagonian Cordillera record HP-MT prograde metamorphic paths (Willner et al., 2004 and Oriolo et al., 2019) while the Cushamen Formation achieves LP-MT conditions (M_1-D_1; ~500°C; < 4.5 Kbars) (Fig. 12b and 14 – Table 6). The prograde metamorphism in the western North Patagonian Massif from greenschist (M_1-D_1) to amphibolite (M_2 - 690 °C; 6.5 Kbars) facies conditions was linked to the Permian arc migration inboard of the Gondwana continent. While the western North Patagonian Massif basement was affected by magmatism and partial melting at MP-HT conditions (M_2), in the Lake Region and Septentrional Patagonian Cordillera the basement developed a retrograde path starting at ~300 Ma (Fig. 13a and 14 – Table 6).

The uplift of the igneous metamorphic basement in the western North Patagonian Massif was linked to the first retrograde metamorphic stage (D_2-S_2) and is possibly simultaneous with the Permian-Triassic retrograde metamorphic path of the Lake Region (Fig. 13b - Table 6). On the other hand, the last retrograde metamorphic stage (D_3) recorded in the Cushamen Formation is possibly correlated with the Jurassic – Cretacic uplift periods (170 – 80 Ma) recorded in the Septentrional Patagonian Cordillera (Oriolo et al., 2019) and the accretionary prism (Willner et al., 2005) (Table 6).

9.3. Late Paleozoic geotectonic evolution of the southwestern Gondwana

A subduction paleotectonic setting has been suggested for the geological process which developed during late Paleozoic times in the southwestern Gondwana region (Forsythe 1982; Cingolani et al., 1991; Martín et al., 1999; Duhart et al., 2001; Lucassen et al., 2004; Willner et al., 2004 and 2005; Cawood, 2005; García-Sansegundo et al., 2009; Cawood et al., 2011; Varela et al., 2015; Oriolo et al., 2019; Gregori et al., 2020, among others). During this time, an accretionary prism and magmatic arcs developed at the boundary of the continental margin, and the sedimentary sequences distributed in the Lake Region, Septentrional Patagonian Cordillera and the western North Patagonian Massif were affected by progressive metamorphism.

The metamorphism, deformation, and magmatism of the late Paleozoic basements progress toward the interior of the Gondwana continent after the sedimentation stage (Fig. 14). This geodynamic evolution might be linked to the progressively shallower dip subduction of the proto-Pacific lithosphere. This slab subduction behavior has at least two possible geotectonic scenarios: (a) A slab breakoff mechanism linked to an early subduction stage and then continental collision (Von Blanckenbur, 1995) or (b) Flat slab subduction, possibly triggered by subduction of oceanic lithosphere plateau, or by subduction of a young proto-Pacific slab with a slow convergence rate (Cloos, 1993; Stern, 2002; Manea et al., 2017).

If the slab breakoff process took place during the late Paleozoic evolution a peak of pressure must have developed before the uplift and thermal peak (Davies and Von Blanckenbur, 1995, and Von Blanckenbur, 1995). Although we cannot define the prograde path from greenschist (M_1-D_1) to amphibolite (M_2) facies conditions, we have no any structural, petrographic, or geothermobarometric results to support this hypothesis. In contrast, the characteristics of the geodynamic evolution in the southwestern Gondwana continent fits better with the flat slab subduction process (Fig. 14). This mechanism develops an HP-MT path in the accretionary prism and fore-arc regions (e.g. Cloos, 1993; Peacock, 1996 and Stern, 2002) and low-medium pressure and medium-high temperature metamorphism conditions inboard of the continental plate (e.g. Collins, 2002 and Gray and Foster, 2004 and references therein).

10. Conclusions

The geological studies carried out on the western North Patagonian basement allow us to make a geodynamic evolution model for the sedimentation, metamorphism, magmatism, and exhumation processes of the late Paleozoic igneous- metamorphic belt. The sedimentation cycle of the Cushamen Formation is the oldest stage and occurred during the Carboniferous Period, taking into account the maximum age of sedimentation, close to 369 ± 8 Ma. The first tectonic-metamorphic event (330-300 Ma?) reached the greenschist facies and produced the main foliation (S_1) of the schist unit. The migmatization and the garnet crystallization record the highest pressure and temperature in amphibolite facies conditions. These facts took place during the second prograde metamorphic stage (~ 290 Ma) and are related to the Permian magmatism represented by the igneous bodies of the Mamil Choique Formation. Two deformation stages (D_2 and D_3) developed during the retrograde metamorphic stage and linked to the uplift of the igneous-metamorphic basement. The second foliation (S_2), linked to F_2 folds, represents the first retrograde metamorphic stage (D_2; 265-235 Ma) developed in greenschist conditions and with NE - SW principal stress (σ_1) compression. The last event (D_3) is characterized by folds (F_3) with wavelengths of hundreds of meters and NNW - SSE orientation for the principal stress component (σ_1). The geochronological correlations between the geodynamic model and the neighboring basements allow us to suggest a flat slab subduction paleotectonic setting for the southwestern Gondwana boundary during late Paleozoic times. Further tests of these basement regions will improve the knowledge of the evolutionary history of the southwestern Gondwana continent.

11. Acknowledgments

We would like to thank the people from Comallo region (J. García, J.M. Garramuño, C. Criado, S. Navarro, N. Contin, R. Hermosilla and their families) that allowed us access to their lands, gave us shelter, and helped throughout many field trips. We warmly acknowledge the reviews by Editor Marco Scambelluri, Juan Otamendi and Alina Tibaldi which improved greatly the original manuscript. We are also grateful for the helpful made by Juan Cruz Martínez and Jorge Dristas and the work-team of the Laboratory of geochronology and radiogenic isotopes (UERJ). We would also like to acknowledge David Gorman, who carefully corrected the previous version of our manuscript. The Configuración Geológica y Geodinámica del sector central de la Comarca Nordpatagónica and Gondwánico y Patagonídico del Macizo Nordpatagónico occidental research projects, granted by the Universidad Nacional del Sur were used during this study. Many thanks to CONICET for there search project Significado y evolución de Los eventos tectonomagmáticos Gondwánicos y Patagonídicos del Norte de Patagonia.

12. References

Basei, M. A. S., Varela, R., Sato, A. M., Siga Jr, O., and Llambías, E. J. 2002. Geocronología sobre rocas del Complejo Yaminué, Macizo Norpatagónico, Río Negro, Argentina. In Actas 15 Congreso Geológico Argentino (Vol. 3, pp. 117-122).

Berman, R. G. 1988. Internally-consistentthermodynamic data forminerals in thesystem Na2O-K2O-CaO-MgO-FeO-Fe2O3-Al2O3-SiO2-TiO2-H2O-CO2. Journal of petrology, 29(2), 445-522.

Berman, R. G. 1991. Thermobarometry using multi-equilibrium calculations; a new technique, with petrological applications. The Canadian Mineralogist, 29(4), 833-855.

Berman, R. G., and Aranovich, L. Y. 1996. Optimized standard state and solution properties of minerals. Contributions to Mineralogy and Petrology, 126(1-2), 1-24.

Berman, R. G., Aranovich, L. Y., Rancourt, D. G., and Mercier, P. H. J. 2007. Reversed phase equilibrium constraints on the stability of Mg-Fe-Al biotite. American Mineralogist, 92(1), 139-150.

Bucher, K. and Grapes, R. 2008. Petrogenesis of metamorphic rocks. Springer Science & Business Media. 428p.

Cawood, P. A. 2005. Terra Australis Orogen: Rodinia breakup and development of the Pacific and Iapetus margins of Gondwana during the Neoproterozoic and Paleozoic. Earth-Science Reviews, 69(3-4), 249-279.

Cawood, P. A., Leitch, E. C., Merle, R. E. and Nemchin, A. A. 2011. Orogenesis without collision: Stabilizing the Terra Australis accretionary orogen, eastern Australia. Bulletin, 123(11-12), 2240-2255.

Cerredo, M.E. 1997. The metamorphism of Cushamen formation, Río Chico area. North Patagonian Massif. Argentina. 8th Congreso. Geológico Chileno, Antofagasta, Actas 2, pp. 1236–1240.

Cerredo, M. E., and López de Luchi, M. G. 1998. MamilChoiqueGranitoids, southwestern North Patagonian Massif, Argentina: magmatism and metamorphism associated with a polyphasic evolution. Journal of South American Earth Sciences, 11(5), 499-515.

Chatterjee, N. D. and Froese, E. 1975. A thermodynamic study of the pseudobinary join muscovite-paragonite in the system $KAlSi_3O_8$-$NaAlSi_3O_8$-Al_2O_3-SiO_2-H_2O. American Mineralogist: Journal of Earth and Planetary Materials, 60(11-12), 985-993.

Cingolani, C., Dalla Salda, L., Hervé, F., Munizaga, F., Pankhurst, R. J., Parada, M. A., and Rapela, C. W. 1991. The magmatic evolution of northern Patagonia; new impressions of pre-Andean and Andean tectonics. Geological Society of America Special Paper, 265, 29-44.

Cloos, M. 1993. Lithospheric buoyancy and collisional orogenesis: Subduction of oceanic plateaus, continental margins, island arcs, spreading ridges, and seamounts. Geological Society of America Bulletin, 105(6), 715-737.

Collins, W. J. 2002. Hot orogens, tectonic switching, and creation of continental crust. Geology, 30(6), 535-538.

Conolly, J. 1990. Multivariable phase diagrams: an algorithm based on generalized thermodynamics. American Journal of Sciences 290, 666–718.

Costa, R.V., Trouw, R.A.J., Mendes, J.C., Geraldes, M., Tavora, A., Nepomuceno, F., Araújo Jr., E.B., 2017. Proterozoic evolution of part of the Embu Complex, eastern São Paulo state, SE Brazil. Journal of South American Earth Sciences, 79, 170-188.

Dalla Salda, L. H., Varela, R., Cingolani, C., and Aragón, E. 1994. The Rio Chico Paleozoic crystalline complex and the evolution of Northern Patagonia. Journal of South American Earth Sciences, 7(3), 377-386.

Davies, J. H., and von Blanckenburg, F. 1995. Slab breakoff: a model of lithosphere detachment and its test in the magmatism and deformation of collisional orogens. Earth and Planetary Science Letters, 129(1-4), 85-102.

Deckart, K., Hervé F., Allamand, F., Fanning, M., Ramírez, V., Calderón, M. and Godoy, E. 2014. U/Pb geochronology and Hf-O isotopes of zircons from the Pennsylvanian Coastal Batholith, south-central Chile.

Duhart, P., McDonough, M., Muñoz, J., Martin, M., and Villeneuve, M. 2001. El Complejo Metamórfico Bahía Mansa en la cordillera de la Costa del centro-sur de Chile (39° 30'-42° 00'S): geocronología K-Ar, 40Ar/39Ar y U/Pb e implicancias en la evolución del margen sur-occidental de Gondwana. Revista geológica de Chile, 28(2), 179-208.

Duhart, P., Haller, M.J., and Hervé, F. 2002. Diamictitas como parte del protolito de las metamorfitas de la Formación Cushamen en Río Chico, provincias de Río Negro y Chubut, Argentina. In Congreso Geológico Argentino (No. 15, pp. 97-100).

Duhart, P., Cardona, A., Valencia, V., Muñoz, J., Quiroz, D., and Hervé, F. 2009. Evidencias de basamento Devónico, Chile centro-sur [41–44S]. In CongresoGeológico Chileno, 12th (Santiago), Abstracts (pp. S8-009).

Ferry, J. T., and Spear, F. S. 1978. Experimental calibration of the partitioning of Fe and Mg between biotite and garnet. Contributions to mineralogy and petrology, 66(2), 113-117.

Forsythe, R. 1982. The late Palaeozoic to early Mesozoic evolution of southern South America: a plate tectonic interpretation. Journal of the Geological Society, 139(6), 671-682.

Fuhrman, M. L., and Lindsley, D. H. 1988. Ternary-feldspar modeling and thermometry. American mineralogist, 73(3-4), 201-215.

García-Sansegundo, J., Farias, P., Gallastegui, G., Giacosa, R. E., and Heredia, N. 2009. Structure and metamorphism of the Gondwanan basement in the Bariloche region (North Patagonian Argentine Andes). International Journal of Earth Sciences, 98(7), 1599.

Geraldes, M.C., Almeida, B.S., Tavares Jr., A., Dussin, I., and Chemale, F., 2015. U/Pb and Lu-Hf calibration of the new LA-ICP-MS Multilab at Rio de Janeiro State University. In: Geoanalysis 2015. Leoben, Geoanalysis.

González, P. D., Poiré, D., and Varela, R. 2002. Hallazgo de trazas fósiles en la Formación El Jagüelito y su relación con la edad de las metasedimentitas, Macizo Nordpatagónico Oriental, Provincia de Río Negro. Revista de la Asociación Geológica Argentina, 57(1), 35-44.

González, P., Coluccia, A., and Franchi, M. 2003. Hoja 4169-III Ingeniero Jacobacci. Carta Geológica de la República Argentina, escala 1, 250.

González, P. D., Sato, A. M., Naipauer, M., Varela, R., Basei, M., Sato, K., Llambías, E., Chemale, F. and Dorado, A. C. 2018. Patagonia-Antarctica Early Paleozoic conjugate margins: Cambrian synsedimentary silicic magmatism, U/Pb dating of K-bentonites, and related volcanogenic rocks. Gondwana Research, 63, 186-225.

Gray, D. R., and Foster, D. A. 2004. Tectonic evolution of the Lachlan Orogen, southeast Australia: historical review, data synthesis and modern perspectives. Australian Journal of Earth Sciences, 51(6), 773-817.

Greco, G. A., González, S. N., Sato, A. M., González, P. D., Basei, M. A., Llambías, E. J., and Varela, R. (2017). The Nahuel Niyeu basin: a Cambrian forearc basin in the eastern North Patagonian Massif. Journal of South American Earth Sciences, 79, 111-136.

Gregori, D. A., Kostadinoff, J., Strazzere, L., and Raniolo, A. 2008. Tectonic significance and consequences of the Gondwanide orogeny in northern Patagonia, Argentina. Gondwana Research, 14(3), 429-450.

Gregori, D. A., Strazzere, L., Barros, M., Benedini, L., Marcos, P. and Kostadinoff, J. 2020. The Mencué Batholith: Permian episodic arc-related magmatism in the western North Patagonian Massif, Argentina. International Geology Review, 1-25.

Guidotti, C V. 1984. Micas in metamorphicrocks. In Mineralogical Society of America Reviews in Mineralogy, 13,357-468.

Hervé, F., Haller, M. J., Duhart, P., and Fanning, C. M. 2005. SHRIMP U–Pb ages of detrital zircons from Cushamen and Esquel Formations, North Patagonian Massif, Argentina: geological implications. In XVI Congreso Geológico Argentino (La Plata), Actas (pp. 309-314).

Hervé, F., Calderón, M., Fanning, C. M., Pankhurst, R. J., and Godoy, E. 2013. Provenance variations in the Late Paleozoic accretionary complex of central Chile as indicated by detrital zircons. Gondwana Research, 23(3), 1122-1135.

Hervé, F., Calderon, M., Fanning, C. M., Pankhurst, R. J., Fuentes, F., Rapela, C. W., and Marambio, C. 2016. Devonian magmatism in the accretionary complex of southern Chile. Journal of the Geological Society, 173(4), 587-602.

Hervé, F., Calderón, M., Fanning, M., Pankhurst, R., Rapela, C. W.and Quezada, P. 2018. The country rocks of Devonian magmatism in the North Patagonian Massif and Chaitenia. Andean Geology, 45(3), 301-317.

Hirth, G., and Tullis, J. 1992. Dislocation creep regimes in quartz aggregates. Journal of structural geology, 14(2), 145-159.

Hodges, K. V., and Crowley, P. T. 1985. Error estimation and empirical geothermobarometry for pelitic systems. American mineralogist, 70(7-8), 702-709.

Hoisch, T. D. 1989. A muscovite-biotite geothermometer. American Mineralogist, 74(5-6), 565-572.

Hoisch, T. D. 1990. Empirical calibration of six geobarometers for the mineral assemblage quartz+ muscovite+ biotite+ plagioclase+ garnet. Contributions to Mineralogy and Petrology, 104(2), 225-234.

Holland, T., and Powell, R. 1991. A compensated Redlich-Kwong equation for volumes and fugacities of CO2 and H2O in the range 1 bar to 50 kbar and 100–1600 °C. Contributions to Mineralogy and Petrology 109, 265–273.

Holland, T.J.B., and Powell, R. 1998. An internally consistent thermodynamic data set forphases of petrological interest. Journal of Metamorphic Geology 16, 309–343.

Koziol, A. M., and Newton, R. C. 1988. Redetermination of the anorthite breakdown reaction and improvement of the plagioclase-garnet-Al_2SiO_5-quartz geobarometer. American Mineralogist, 73(3-4), 216-223.

Lavrent'eva, I. V. and Perchuk, L. L. 1981. Phase correspondence in the biotite-garnet system-experimental-data.Doklady Akademii Nauk SSSR, 260(3), 731-734.

López de Luchi, M. L., Cerredo, M. E. and Wemmer, K. 2006. Time constraints for the tectonic evolution of the SW corner of the North Patagonian Massif, Argentina. In Fifth South American Symposium on Isotope Geology, Punta del Este, Uruguay Short Papers (Vol. 221).

Lucassen, F., Trumbull, R., Franz, G., Creixell, C., Vásquez, P., Romer, R. L. and Figueroa, O. 2004. Distinguishing crustal recycling and juvenile additions at active continental margins: the Paleozoic to recent compositional evolution of the Chilean Pacific margin (36–41 S). Journal of South American Earth Sciences, 17(2), 103-119.

Ludwig, K. R. 2003. Isoplot 3.00: A geochronological toolkit for Microsoft Excel. Berkeley Geochronology Center Special Publication, 4, 70.

Manea, V. C., Manea, M., Ferrari, L., Orozco-Esquivel, T., Valenzuela, R. W., Husker, A., and Kostoglodov, V. 2017. A review of the geodynamic evolution of flat slab subduction in Mexico, Peru, and Chile. Tectonophysics, 695, 27-52.

Marcos, P., Gregori, D. A., Benedini, L., Barros, M., Strazzere, L. and Pivetta, C. P. 2018. Pennsylvanian glacimarine sedimentation in the Cushamen Formation, western North Patagonian Massif. Geoscience Frontiers, 9(2), 485-504.

Martin, M. W., Kato, T. T., Rodriguez, C., Godoy, E., Duhart, P., McDonough, M., and Campos, A. (1999). Evolution of the late Paleozoic accretionary complex and overlying forearc-magmatic arc, south central Chile (38°–41° S): Constraints for the tectonic setting along the southwestern margin of Gondwana. Tectonics, 18(4), 582-605.

Martínez, J. C., Dristas, J. A., Massonne, H. J. 2012. Palaeozoic accretion of the microcontinent Chilenia, North Patagonian Andes: high-pressure metamorphism and subsequent thermal relaxation. International Geology Review, 54(4), 472-490.

Martínez, J. C., Massonne, H. J., Frisicale, M. C., and Dristas, J. A. 2017. Trans-Amazonian U-Th-Pb monazite ages and PTd exhumation paths of garnet-bearing leucogranite and migmatitic country rock of the southeastern Tandilia belt, Rio de la Plata craton in Argentina. Lithos, 274, 328-348.

Massonne, H. J., Dristas, J. A., and Martínez, J. C. 2012. Metamorphic evolution of the Río de la Plata craton in the Cinco Cerros area, Buenos Aires Province, Argentina. Journalof South American EarthSciences, 38, 57-70.

Oriolo, S., Schulz, B., González, P. D., Bechis, F., Olaizola, E., Krause, J., Renda E. and Vizán, H. 2019. The Late Paleozoic tectonometamorphic evolution of Patagonia revisited: Insights from the pressure-temperature-deformation-time (P-T-D-t) path of the Gondwanide basement of the North Patagonian Cordillera (Argentina). Tectonics.

Pankhurst, R. J., Rapela, C. W., Fanning, C. M., and Márquez, M. 2006. Gondwanide continental collision and the origin of Patagonia. Earth-Science Reviews, 76 (3), 235-257.

Pankhurst, R.J., Rapela, C.W., De Luchi, M.L., Rapalini, A.E., Fanning, C.M., and Galindo, C. 2014. The Gondwana connections of northern Patagonia. Journal of the Geological Society 171 (3), 313 - 328.

Passchier, C. W., and Trouw, R. A. 2005. Microtectonics. Springer Science & Business Media. 371p.

Peacock, S. M. 1996. Thermal and petrologic structure of subduction zones. Subduction: top to bottom, 96, 119-133.

Perchuk, L. L., and Lavrent'eva, I. V. 1983. Experimental investigation of exchange equilibria in the system cordierite-garnet-biotite. In Kinetics and equilibrium in mineral reactions (pp. 199-239). Springer, New York.

Perchuk, L. L., Aranovich, L. Y., Podlesskii, K. K., Lavrent'eva. I. V., Gerasimov. V. Y., Fed'Kin, V. V., Kitsul, V. I.,Karasakov, L. P., and Berdnikov, N. V. 1985. Precambrian granulites of the Aldan shield, eastern Siberia, USSR. Journal of metamorphic Geology, 3(3), 265-310.

Ramos, V. A. 1984. Patagonia: un continente paleozoico a la deriva?. In 9° Congreso Geologico Argentino, SC Bariloche, Buenos Aires, 1984 (pp. 311-325).

Ramos, V. A., García Morabito, E., Hervé, F., y Fanning, C. M. 2010. Grenville-age sources in Cuesta de Rahue, northern Patagonia: constrains from U–Pb/SHRIMP ages from detrital zircons. In International Geological Congress on the Southern Hemisphere (pp. 42-44). Mar del Plata, Argentina.

Rapalini, A. E., López de Luchi, M., Martínez Dopico, C., Lince Klinger, F., Giménez, M., and Martínez, P. 2010. Did Patagonia collide with Gondwana in the Late Paleozoic? Some insights from a multidisciplinary study of magmatic units of the North Patagonian Massif. Geologica Acta, 8(4), 0349-371.

Rapalini, A. E., Luchi, M. L., Tohver, E., and Cawood, P. A. 2013. The South American ancestry of the North Patagonian Massif: geochronological evidence for an autochthonous origin?. Terra Nova, 25(4), 337-342.

Reche, J. and Martinez, F. J. 1996. GPT: an Excel spreadsheet for thermobarometric calculations in metapelitic rocks. Computers & Geosciences, 22(7), 775-784.

Rieder, M., Cavazzini, G., D'yakonov, Y. S., Frank-Kamenetskii, V. A., Gottardi, G., Guggenheim, S., Koval, P. V., Müller, G., Neiva, A. M. R., Radoslovich, E. W., Robert, J. L., Sassi, F. P., Takeda, H., Weiss, Z., and Wones, D. R., 1998. Nomenclature of the micas. Clays and clay minerals. 46(5), 586-595.

Sawyer, E. W., 2008. Working with migmatites (Vol. 38). Mineralogical Association of Canada. 168p.

Serra-Varela, S., González, P., Giacosa, R., Heredia, N., Pedreira, D., Martín-González, F. and Sato, A. 2019. Evolution of the Palaeozoic basement of the Northpatagonian Andes in the San Martín de los Andes area (Neuquén, Argentina): Petrology, age and correlations. Andean Geology, 46(1).

Stern, R. J. 2002. Subduction zones. Reviews of geophysics, 40(4), 3-1.

Suárez, R., González, P. D., and Ghiglione, M. C. 2019. A review on the tectonic evolution of the Paleozoic-Triassic basins from Patagonia: Record of protracted westward migration of the pre-Jurassic subduction zone. Journal of South American Earth Sciences, 102256.

Varela, R., Cingolani, C., Sato, A., Dalla Salda, L., Brito Neves, B. B., Basei, M. Siga Jr., and Teixeira, W. 1997. Proterozoic and paleozoic evolution of Atlantic area of North-Patagonian Massif, Argentine. In South-American Symposium on Isotope Geology (pp. 326-328).

Varela, R., Basei, M. A. S., Sato, A. M., Siga Jr, O., Cingolani, C., and Sato, K. 1998. Edades isotópicas Rb/Sr y U/Pb en rocas de Mina Gonzalito y Arroyo Salado. In Macizo Norpatagónico Atlántico, Río Negro, Argentina. Buenos Aires, 10 Congreso Latinoamericano de Geología y 6 Congreso Nacional de Geología Económica (Vol. 1, pp. 71-76).

Varela, R., Basei, M. A., Brito Neves, B. B., Sato, A. M., Teixeira, W., Cingolani, C. A., and Siga Jr, O. 1999. Isotopic study of igneous and metamorphic rocks of Comallo - Paso Flores, Río Negro, Argentina. In South American Symposium on Isotope Geology (Vol. 2, pp. 148-151).

Varela, R., Basei, M. A., Cingolani, C. A., Siga Jr, O., and Passarelli, C. R. 2005. El basamento cristalino de los Andes norpatagónicos en Argentina: geocronología e interpretación tectónica. Revista geológica de Chile, 32 (2), 167-187.

Varela, R., Gregori, D., González, and P. D., and Basei, M. A. 2015. Caracterización geoquímica del magmatismo de arco devónico y carbonífero pérmico en el noroeste de Patagonia, Argentina. Revista de la Asociación Geológica Argentina, 72 (3), 419-432.

Volkheimer, W. 1973. Observaciones geológicas en el área de Ingeniero Jacobacci y adyacencias (Provincia de Río Negro). Revista de la Asociación Geológica Argentina, 28 (1), 13-37.

Von Blanckenburg, F., and Davies, J. H. 1995. Slab breakoff: a model for syncollisional magmatism and tectonics in the Alps. Tectonics, 14(1), 120-131.

Von Gosen, W. 2009. Stages of Late Palaeozoic deformation and intrusive activity in the western part of the North Patagonian Massif (southern Argentina) and their geotectonic implications. Geological magazine, 146 (1), 48.

Whitney, D. L., and Evans, B. W. 2010. Abbreviations for names of rock-forming minerals. American mineralogist, 95(1), 185-187.

Willner, A. P., Glodny, J., Gerya, T. V., Godoy, E., and Massonne, H. J. 2004. A counterclockwise PTt path of high-pressure/low-temperature rocks from the Coastal Cordillera accretionary complex of south-central Chile: constraints for the earliest stage of subduction mass flow. Lithos, 75(3-4), 283-310.

Willner, A. P., Thomson, S. N., Kröner, A., Wartho, J. A., Wijbrans, J. R. and Hervé, F. 2005. Time markers for the evolution and exhumation history of a Late Palaeozoic paired metamorphic belt in North–Central Chile (34–35 30′ S). Journal of Petrology, 46(9), 1835-1858.

Figure captions

Fig. 1: Geological sketch map showing the basement outcrops of the Lake Region (Chile), Septentrional Patagonian Cordillera, Neuquén Basin, Extra-Andean Chubut and North Patagonian Massif between 39° S and 44° S (modified from Marcos et al., 2018 and references therein).

Fig. 2: Geological sketch of the western North Patagonian basement units in the Comallo locality. The lower hemisphere equal area stereoplot projections of poles represent: Main foliation (S_1) in the railroad track (I), National Route N°23 (II), and Comallo creek (III) outcrops. Fold axes orientation related to the second (F_2-IV) and the last (F_3-I) deformation stages during the retrograde metamorphism. (V) Foliation orientation of Mamil Choique granitoid outcrops related to the second deformation stage (D_2).

Fig. 3: (a) Mica and quartz-mica schist sequences intruded by dikes of Neneo Ruca Formation on the railroad track. (b) Foliated igneous bodies of Mamil Choique Formation related to the second stage deformation (D_2) along the eastern railroad track outcrops. (c) Paleosome and leucosome differentiation in the Comallo creek outcrops. (d) Folds (F_2) developed in the stromatic migmatites lithofacies. The arrows distinguish the biotite-rich thin bands of the melanosome, leucosome, and paleosome layers. (e) Isoclinal folds (F_2) with NW-SE fold axes orientation of the quartz-mica schists correspond to the western National Route 23 outcrops.

Fig. 4: Photomicrographs of the metamorphic lithofacies with the most important textures features. (a) Detail of the ribbon quartz and lepidoblastic thin layers of the mica-schists lithofacies. Three quartz grains have intercrystalline twistwall subtype-texture. (b) Mica-schist lithofacies with textural attributes correspond to: main foliation (S_1) associated with the first tectonic-metamorphic event (M_1-D_1); second foliation (S_2) linked to the second deformation event (D_2). (c) Microfolds of quartz aggregates and lepidoblastic microbands linked to the D_2 deformation event. (d) S_1 and S_2 foliations preserved in the quartz-mica-garnet schist lithofacies (e) Quartz-mica schist lithofacies with lepidogranoblastic arrangement, twistwall subtype quartz textures (middle sector) and neoformation of quartz along the boundary relicts grains (middle-lower sector). (f) Chessboard and twistwall sub-type microtextures inside quartz grains of the stromatic migmatites lithofacies. (g) Paleosome of stromatic migmatites lithofacies shows porphyroblastic textures and high content of garnet.

Fig. 5: P-T diagrams obtained with TWQ of the geothermometer and geobarometer intersection reactions of the P49 and P7 samples. The P-T results for the garnet and plagioclase cores composition are plot in red dots and rims compositions in green dots. (a) Quartz-mica-garnet schist (sample 49) with GrtBt (R2) – GBP (R3) intersections plots. (b-c-d) Stromatic migmatite P-T diagrams with the following intersections: (b) GrtBt (R2) – GBP (R3); (c) GrtBt (R2) – GASP (R4) (d) GrtBt (R2) – GBSQ (R5).

Fig. 6: P-T diagrams of the quartz-mica schist lithofacies (sample P35) from the railroad tracks western outcrops calculated in the system Mn–NCKFMASHTO with the Perple_X software package (Connolly 1990). (a) P-T pseudosection with the different stability fields of mineral components. The ascending colors in violet intensity refer to the increase in the degree of freedom that varies from two to seven. (b) P-T diagram with garnet, biotite, and muscovite curve stability and isopleths Si (a.p.f.u) content of muscovite.

Fig. 7: P-T diagrams of the quartz-mica-garnet schist lithofacies (sample P49) from the National Route 23 eastern outcrops calculated in the system Mn–NCKFMASHTO with the Perple_X software package (Connolly 1990). (a) P-T pseudosection with the different stability fields of mineral components. The ascending colors in violet intensity refer to the increase in the degree of freedom that varies from two to seven. (b) P-T diagram with isopleths molar fraction of Mg and Ca in garnets and Si (a.p.f.u) content in biotite. The X_{Mg} and X_{Ca} intersections for the garnet cores composition are plot in red dots and rims compositions intersection in green dots.

Fig. 8: P-T diagrams of the stromatic migmatites lithofacies (sample P7) from the railroad track eastern outcrops calculated in the system Mn–NCKFMASHTO with the Perple_X software package (Connolly 1990). (a) P-T pseudosection with the different stability fields of mineral components. The ascending colors in violet intensity refer to the increase in the degree of freedom that varies from two to six. (b) P-T diagram with isopleths molar fraction of Mg and Ca in garnet and the

weight % of garnet in the modeled sample. The X_{Mg} and X_{Ca} intersections for the garnet cores composition are plot in red dots and rims compositions intersection in green dots.

Fig. 9: U/Pb detrital zircon ages of the quartz-mica schist lithofacies (sample PC44D). (a) CL image of prismatic-subrounded selected zircon grains with the location of the analyzed spots (Table C - supplementary data). (b) Ninety-four (94) analyses displayed on the Tera-Wasserburg diagram with a 95% confidence limit error ellipses. Each analysis has a concordance percentage equal or better than 90% and error ellipse lesser than 10%. (c) Relative probability plot (dark curves) and frequency histogram (grey bars) of detrital zircon ages. Numbers over the curves are ages of probability peaks and color bars represent the ages of the populations of zircon grains. (d) Detail of Neoproterozoic - Paleozoic detrital zircon ages displayed on a frequency histogram (grey bars) with the relative probability curve. Paleozoic peaks and the maximum depositional age are represented by weighted-mean age (n= number of detrital zircon employed for the calculation).

Fig. 10: Block diagrams of the late Paleozoic evolution stages for the western North Patagonian Massif basement.

Fig. 11: P-T diagram showing the exhumation path of the garnet-bearing lithofacies. Core garnets compositions correspond to the arrow bases (red color) while the rim garnet compositions represent the arrowheads (green color).

Fig. 12: Block diagrams of the Carboniferous stages between 39°S and 44°S. (a) Paleogeographic configuration for the Carboniferous sedimentation stage along the western North Patagonian, Septentrional Patagonian Cordillera, Extra-andean Chubut and Lake Region. (b) Paleogeographic sketch for the Caboniferous magmatism and the first tectonic-metamorphism event for the late Paleozoic units. The different paleotectonic segments and their boundaries are not in scale.

Fig. 13: Block diagrams of the Permian-Triassic stages between 39°S and 44°S. (a) Paleogeographic distribution of the Permian magmatism and their tectonic-metamorphic setting. (b) Diagram showing the last stage evolution for the late Paleozoic basement with the final lapse of the exhumation history over Mesozoic times. The different paleotectonic segments and their boundaries are not in scale.

Fig. 14: Paleotectonic reconstruction and P-T path for the southwestern Gondwana boundary during late Paleozoic.

Fig. A: $^{206}Pb/^{238}U$ versus $^{207}Pb/^{235}U$ diagram showing the Concordia line and Concordia age for the secondary standard (91500).

Fig. B: Chemical profiles for garnets of the stromatic migmatite (sampe P7) and the quartz-mica-garnet schist (sample P49) lithofacies.

Table 1: Mineral associations of the mica-schist, quartz-mica schist, quartz-mica-garnet schist, and stromatic migmatite lithofacies. Nomenclature of the minerals following the classification of Whitney and Evans (2010).

Lithofacies	***Mineral association***					
	Prograde metamorphism			***Retrograde metamorphism***		
	MAA (Qz+Ms+Bt+Pl±Chl)	**MAB** (Qz+Ms+Bt+Pl+Grt)	**MAC** (Qz+Ms+Bt+Pl+Grt±Sil)	**MAD** (Qz+Ms)	**MAE** (Qz+Ms+Bt)	**MAF** (Chl+Src)
Mica schist	-----------			-----------		-----------
Quartz-mica schist	-----------				-----------	-----------
Quartz-mica-garnet schist	-----------	-----------			-----------	-----------
Stromatic migmatites	-----------	-----------	-----------			-----------

Table 2: Representative electron microprobe analyses of biotite, muscovite, plagioclase and garnet in the quartz-mica schist (P35), quartz-mica-garnet schist (P49) and stromatic migmatite (P7).

	P49							P7						
	Bt	Bt (i)	Ms	Pl		Grt		Bt	Bt (i)	Ms	Pl		Grt	
Rim				Core	Rim	Core	Rim				Core	Rim	Core	Rim
0.62	34.73	34.27	47.70	60.66	60.66	37.61	37.54	35.23	34.19	47.56	59.89	60.33	37.29	37.33
0.01	1.73	2.67	0.70	0.01	0.13	0.01	0.03	2.06	2.15	0.36	0.00	0.00	0.01	0.01
4.69	18.67	18.56	36.44	25.46	23.75	20.88	21.04	18.69	18.31	36.83	24.54	24.11	20.85	20.84
0.02	0.08	0.00	0.04	0.02	0.03	0.03	0.02	0.04	0.02	0.04	0.03	0.00	0.04	0.01
0.05	0.00	0.00	1.02	0.07	0.18	0.07	0.22	0.43	0.00	0.91	0.12	0.04	0.96	0.61
0.00	20.87	21.36	0.99	0.00	0.00	33.65	33.63	21.91	21.23	0.75	0.00	0.00	33.44	33.87
0.02	0.10	0.18	0.03	0.03	0.12	3.86	4.41	0.35	0.41	0.01	0.03	0.02	3.40	3.65
0.03	8.69	8.31	0.84	0.09	0.20	2.78	2.17	8.22	7.47	0.94	0.02	0.02	3.39	2.98
6.52	0.00	0.00	0.00	6.40	4.69	1.35	1.73	0.00	0.00	0.00	6.23	5.27	1.25	1.24
3.16	0.13	0.11	0.55	7.85	8.71	0.00	0.00	0.09	0.15	0.53	8.87	9.36	0.00	0.00
0.17	11.49	11.80	10.65	0.12	0.29	0.00	0.00	10.34	10.84	9.78	0.27	0.29	0.00	0.00
00.28	96.49	97.26	98.98	100.70	100.22	100.22	100.79	97.35	94.75	97.71	99.98	99.44	100.63	100.53
2.69	2.67	2.63	3.06	2.68	2.70	3.02	3.01	2.68	2.68	3.07	2.68	2.71	2.99	3.00
0.00	0.10	0.15	0.03	0.00	0.00	0.00	0.00	0.12	0.13	0.02	0.00	0.00	0.00	0.00
1.29	1.33	1.37	0.94	1.33	1.25	1.98	1.99	1.32	1.32	0.95	1.29	1.28	1.97	1.97
	0.36	0.31	1.81					0.35	0.37	1.85				
0.00	0.01	0.00	0.00	0.00	0.00	0.00	0.00	0.00	0.00	0.00	0.00	0.00	0.00	0.00
0.00	0.00	0.00	0.05	0.00	0.06	0.00	0.01	0.00	0.00	0.04	0.00	0.00	0.06	0.04
0.00	1.34	1.37	0.05	0.00	0.00	2.20	2.26	1.39	1.39	0.04	0.00	0.00	2.24	2.28
0.00	0.01	0.01	0.00	0.00	0.00	0.26	0.30	0.02	0.03	0.00	0.00	0.00	0.23	0.25
0.00	1.00	0.95	0.08	0.01	0.01	0.33	0.26	0.93	0.87	0.09	0.00	0.00	0.40	0.36
0.31	0.00	0.00	0.00	0.30	0.22	0.12	0.15	0.00	0.00	0.00	0.30	0.25	0.11	0.11
0.70	0.02	0.02	0.07	0.67	0.75	0.00	0.00	0.01	0.02	0.07	0.77	0.81	0.00	0.00
0.01	1.13	1.16	0.87	0.01	0.02	0.00	0.00	1.00	1.08	0.80	0.02	0.02	0.00	0.00
	0.43	0.41						0.40	0.39					
0.69				0.68	0.76						0.71	0.75		
						0.761	0.761						0.751	0.762
						0.112	0.087						0.135	0.119
						0.089	0.102						0.077	0.083
						0.039	0.051						0.036	0.036

* Bt: Normalized to 11 oxígens y 8 cations; Ms: Normalized to 11 oxígens y 7 cations; Pl: Normalized to 8 oxígens y 5 cations; Grt: Normalized to 12 oxígens y 8 cations.

Table 3: Bulk-rock compositions (in wt.%) of quartz-mica schist (P35), quartz-mica-garnet schist (P49) and stromatic migmatite (P7). The simplified compositions (*) to the 11-components system Mn-NCKFMASHTO were used for the Perplex_X calculations.

Sample	P35	P35*	P49	P49*	P7	P7*
Oxides						
SiO_2	66.58	66.26	66.30	66.20	55.87	56.83
Al_2O_3	14.36	14.29	15.39	15.37	18.76	19.08
Fe_2O_3	6.20	-	5.67	-	13.18	-
FeO_2	-	5.55	-	5.09	-	12.06
MnO	0.09	0.09	0.06	0.06	0.81	0.82
MgO	2.63	2.62	2.02	2.02	2.73	2.78
CaO	2.66	2.45	2.16	1.96	0.76	0.61
Na_2O	2.63	2.62	2.86	2.86	0.70	0.71
K_2O	2.73	2.72	3.09	3.09	4.45	4.53
TiO_2	0.78	0.78	0.74	0.74	0.50	0.51
P_2O_5	0.15	-	0.15	-	0.12	-
O_2	-	0.03	-	0.03	-	0.07
H_2O		2.60		2.60		2.00
Total	92.61	100	98.44	100	97.88	100

Table 4: Possible geothermometers (R1-R2) and geobarometers (R3-R4-R5) reactions. Thermodynamic calibrations applied in the Excel spreadsheet GPT: (R1) Hoisch (1989); (R2) Ferry and Spear (1978), Lavrent´eva and Perchuk (1981), and Perchuk et al., (1983 and 1985); (R3) Hoisch (1990); (R4) Hodges and Crowley (1985) and Koziol and Newton (1988) (Table B - supplementary data). In the TWQ was employed the thermodynamic equations of Berman (1988), and solid solution models of Berman and Aranovich (1996) for garnet, Berman et al., (2007) for biotite, Fuhrman and Lindsley (1988) for plagioclase and Chatterjee and Froese (1975) for muscovite (R5).

Geothermometers	(R1) Phlogopite + muscovite = aluminoceladonite + eastonite (Mg-Tschermak)
	(R2) Almandine + phlogopite = pyrope + annite (Grt-Bt)
Geobarometers	(R3) Anortite + annite/phlogopite = almandine/pyrope + grossular + muscovite (GBP)
	(R4) Anortite = grossular + quartz + sillimanite (GASP)
	(R5) Almandine/pyrope + muscovite = annite/phlogopite + sillimanite + quartz (GBSQ)

Table 5: Average geothermobarometry results obtained with TWQ, GPT Excel spreadsheet, and Perple_X for the quartz-mica schist (P35), quartz-mica-garnet schist (P49) and stromatic migmatite (P7).

Sample	Program	Geotermometer Geobarometer	CORE				RIM		
			Temperature (°C)		Pressure (bars)		Temperature (°C)		Press
			Average	Std. Deviation	Average	Std. Deviation	Average	Std. Deviation	Averag
P7	TWQ	GrtBt-GASP	697	14	5402	297	653	13	5335
		GrtBt-GBSQ	702	15	6371	570	651	11	5554
		GrtBt-GBP	698	14	5594	332	651	11	5416
	GPT	Grt-Bt	698	9	-	-	649	21	-
		GASP	-	-	5705	315	-	-	4972
		GBP	-	-	5446	335	-	-	4486
	PERPLEX	X_{Mg}-X_{Ca} (Grt)	690	8	6687	233	655	7	5967
P49	TWQ	GrtBt-GBP	593	12	3638	170	556	20	3608
	GPT	Grt-Bt	629	10	-	-	559	16	-
		GBP	-	-	4138	396	-	-	4188
	PERPLEX	X_{Mg}-X_{Ca} (Grt)	658	8	5541	139	601	42	4881
P35	GTP	Bt-Ms	517	9	-		-		
	PERPLEX	X_{Si}Ms	450-600		< 4000		-		

* Core and rim correspond to the plagioclase and garnet compositions.

Table 6: Summary of the deformation, metamorphism, and magmatism stages recognized for the late Paleozoic igneous - metamorphic belts. The characteristics and ages of these events follow: (a) Western North Patagonian Massif: Volkheimer (1973), Dalla Salda et al., (1994), Varela et al., (1999, 2005 and 2015), González et al., (2003) Lopez de Luchi et al., (2006), Pankhurst et al., (2006); Von Gosen (2009) and Gregori et al., (2020). (b) Septentrional Patagonian Precordillera: García-Sansegundo et al., (2009), Oriolo et al., (2019). (c) Lake Region: Duhart et al., (2001), Willner et al., (2004 and 2005), Deckart et al., (2014). The units between the middle Permian to Cretacic are not represented in the table.

Time	Western North Patagonian Massif						Septentr…
	Comallo				Río Chico - Mamil Choique - Cushamen		
	This work		Previous works				
	Deformation - Metamorphism	Magmatism	Deformation - Metamorphism	Magmatism	Deformation - Metamorphism	Magmatism	Deformatio… Metamorph…
Mesozoic	D_3 - Open folds (F_3); ENE-WSW fold axes orientation; NNW-SSE compression (~345°)	-	-	-	D_4 - folding phase with NE-SW fold axes orientation	-	D_3 - Open f… (F_3) and sh… zones (T: 48… P: 2 Kbars-… 80 Ma)
Permian	D_2 - Isoclinal and open folds (F_2); NW-SE thrust fault; S_2 foliation of Cushamen Fm. and foliation of Mamil Choique Fm.; NE-SW compression (~230°); greenschist facies (T: 500 - 300 °C P: 5 - 1 Kbars)	-	D_3 - Open folds (F_3); shear zones (C_3); S_1 foliations in Mamil Choique Fm.; NE-SW compression; greenschist facies (265-235 Ma)	-	D_3 - Open folds (F_3); shear zones (C_3); S_1 foliations in mamil Choique; NW-SE and E-W compression; greenschist facies (272-265 Ma)	-	-
	M_2 - Migmatization and garnet-bearing lithofacies in deepest schist sequences - amphibolite facies (T: 690 °C P: 6.5 Kbars)	Granodiorite bodies of the Mamil Choique Fm. (ca. 290 Ma)	Metamorphic event with thermal input and grow of garnet-bearing mica-schists	Granodiorites and tonalites (290 Ma -279 Ma) of the Mamil Choique Fm.	-	Granodiorites, tonalites (295 - 281 Ma.), granites (ca. 272 Ma) of the Mamil Choique Fm.	-
Carboniferous	M_1-D_1 - Main foliation with N330°/30°SW and N20°/30°NW in Cushamen Fm., greenschist facies (T: 500 °C P: < 4.5 Kbars)	-	D_2 - S_2 main foliation; E -W and NE-SW compression; upper greenschist facies	-	D_2 - S_2 main foliation; W-E and NE-SW compression; upper greenschist facies (335-300 Ma)	Carboniferous granitoids (330-314 Ma)	D_2- S_2 folia… WNW-ESE… NNW-SSE s… isoclinals fo… F_2; metamo… peak (T: 65… P: 11 Kbar… 302 Ma)
	-	-	-	-	D_1- S_1 foliation recognized as folded inclusion in porphyroblast; greenschist facies		D_1-S_1 an… isoclinal fol… (F_1); (T: 400… °C P: 7 Kba…

Table A: LA-MC-ICPMS U/Pb results of the secondary standard 91500.

Secondary Standard	f_{206}[a]	Pb	Th	U	Isotope ratios										
		ppm	ppm	ppm	Th/U[b]	$^{207}Pb/^{235}U$	1 s [%]	$^{206}Pb/^{238}U$	1 s [%]	Rho[d]	$^{207}Pb/^{206}Pb$[e]	1 s [%]	$^{207}Pb/^{235}U$	1 s abs	$^{206}Pb/^{238}U$
91500	0.015	8.20	12.32	35.09	0.35	2.00	2.45	0.18	1.51	0.62	0.08	1.92	1114	16.5	1068.1
91500	0.015	11.22	16.80	46.61	0.36	1.90	1.96	0.18	1.03	0.53	0.08	1.67	1081.5	13	1052.8
91500	0.016	14.72	20.04	56.75	0.35	1.91	2.53	0.17	2.20	0.87	0.08	1.25	1083.9	16.9	1038.2
91500	0.014	12.60	18.12	52.10	0.35	1.85	2.13	0.18	1.25	0.59	0.07	1.73	1062.9	14	1060.8
91500	0.012	6.76	11.59	33.90	0.34	1.66	3.14	0.17	2.34	0.75	0.07	2.09	992.6	19.9	1034.4
91500	0.011	7.63	11.61	32.16	0.36	2.07	3.29	0.18	1.92	0.58	0.08	2.68	1139.8	22.6	1090.4
91500	0.009	9.44	15.39	52.42	0.29	1.73	3.74	0.17	1.75	0.47	0.07	3.31	1019.7	24.1	1006.4
91500	0.016	11.14	16.01	44.76	0.36	2.02	4.11	0.18	1.84	0.45	0.08	3.68	1122.5	27.9	1059.2
91500	0.016	11.70	16.98	48.84	0.35	1.98	3.45	0.19	1.52	0.44	0.07	3.10	1108.4	23.3	1129.9
91500	0.012	10.63	17.77	49.75	0.36	1.97	3.71	0.18	1.76	0.48	0.08	3.26	1104.5	25	1077.1
91500	0.012	11.51	19.26	51.70	0.37	2.10	3.18	0.19	2.02	0.64	0.08	2.45	1148.2	21.9	1123
91500	0.016	12.86	18.32	51.74	0.35	2.13	3.93	0.20	1.77	0.45	0.08	3.51	1158.4	27.2	1181.7
91500	0.016	5.34	9.83	28.77	0.34	2.13	4.12	0.20	2.75	0.67	0.08	3.07	1157.8	28.5	1186.5
91500	0.016	13.83	16.23	50.88	0.32	2.09	3.78	0.20	2.87	0.76	0.08	2.46	1144.8	25.9	1168.3
91500	0.015	4.68	7.61	22.43	0.34	2.51	6.30	0.22	3.00	0.48	0.08	5.55	1275.1	45.8	1258

Table B: Geothermobarometry results obtained in the GTP spreadsheet.

Sample	P49		P7	
	core	rim	core	rim
Geothermometers				
Garnet-Biotite (Grt-Bt)				
Ferry and Spear (1978)	643	530.5	707	687
Lavrent´eva and Perchuk, 1981	634	570.8	702	625
Perchuk and Lavrent´eva (1983a)	627	565.9	694	649
Perchuk and Lavrent´eva (1983b)	623	561.5	690	645
Perchuk and Lavrent´eva (1983b)	615	552.8	682	637
Perchuk et al., (1985)	632	573.1	698	652
Average (°C)	629	559	698	649
Standard deviation (°C)	10	16	9	21
Geobarometers				
Garnet-Biotite-Plagioclase (GBP)				
Hoisch (1990)a	4258	4178	5824	4720
Hoisch (1990)b	4018	4198	5069	4253
Average (bars)	4138	4188	5446	4486
Standard deviation	390	623	335	318
Grt-Sill-Qtz-Pl (GASP)				
Hodges and Crowley (1985)	-	-	5572	4802
Koziol and Newton (1988)	-	-	5959	5142
Average (bars)	-	-	5765	4972
Standard deviation (bars)	-	-	315	313

* Core and rim correspond to the plagioclase and garnet compositions.

Table C: U/Pb detrital zircon analyses of the quartz-mica schist (sample PC44D). The nomenclature of each spot, it is a combination of the number spot and the measurement cycle (letters).

PC44D					Isotope ratios								
Spot	***ƒ*** $_{206}$ ^{a}	**Pb**	**Th**	**U**	**Th/U**^{b}	^{207}**Pb**	**1 s [%]**	^{206}**Pb**	**1 s [%]**	**Rho**^{d}	^{207}**Pb**	**1 s [%]**	^{206}**Pb**
		ppm	**ppm**	**ppm**		^{235}**U**		^{238}**U**			^{206}**Pb**^{e}		^{238}**U**
1A	0.016	8.73	10.36	35.96	0.288	1.644	6.50	0.162	5.75	0.885	0.074	3.02	966
2A	0.018	42.00	28.82	422.50	0.068	0.504	9.84	0.065	9.06	0.921	0.056	3.84	409
4A	0.018	70.16	101.98	329.98	0.309	1.628	7.01	0.164	6.37	0.908	0.072	2.94	976
5A	0.016	32.87	284.83	292.59	0.973	0.603	8.70	0.077	7.83	0.901	0.057	3.78	480
6A	0.024	77.54	25.98	152.51	0.170	10.16	8.30	0.438	8.01	0.965	0.168	2.18	2343
8A	0.016	13.77	21.48	58.19	0.369	2.931	9.09	0.235	5.09	0.560	0.090	7.53	1363
9A	0.016	49.89	96.02	159.11	0.604	3.039	3.61	0.254	2.78	0.771	0.087	2.30	1457
1B	0.017	59.20	149.63	548.04	0.273	0.620	4.28	0.078	3.75	0.876	0.058	2.06	481
4B	0.016	20.92	85.15	185.20	0.460	0.614	4.29	0.078	3.83	0.894	0.057	1.92	484
5B	0.016	73.25	98.56	260.38	0.379	2.008	9.90	0.184	2.60	0.263	0.079	9.56	1088
6B	0.017	70.39	134.70	296.60	0.454	1.958	2.86	0.181	1.79	0.626	0.079	2.23	1070
7B	0.016	40.46	159.72	349.61	0.457	0.597	4.66	0.076	4.32	0.927	0.057	1.75	470
8B	0.014	37.93	624.71	305.58	2.044	0.558	3.58	0.071	3.20	0.895	0.057	1.60	442
9B	0.016	16.77	36.02	48.37	0.745	3.915	3.36	0.274	2.63	0.784	0.104	2.09	1560
1C	0.017	28.52	107.64	264.60	0.407	0.647	4.42	0.080	3.83	0.868	0.059	2.19	497
2C	0.016	46.13	397.46	383.25	1.037	0.599	5.13	0.077	4.84	0.944	0.056	1.69	478
3C	0.016	46.25	334.40	395.63	0.845	0.654	4.14	0.083	3.67	0.888	0.057	1.91	516
4C	0.017	31.73	143.40	295.76	0.485	0.592	4.84	0.076	4.34	0.895	0.057	2.16	472
5C	0.016	37.04	289.40	310.44	0.932	0.707	4.46	0.086	3.74	0.839	0.059	2.43	533
6C	0.016	19.59	56.39	60.65	0.930	2.250	6.96	0.201	5.11	0.734	0.081	4.73	1178
9C	0.017	43.47	25.07	510.67	0.049	0.587	6.37	0.074	6.22	0.976	0.057	1.38	463
1D	0.017	30.23	77.91	283.70	0.275	0.591	4.40	0.076	4.04	0.917	0.056	1.75	474
2D	0.017	27.58	19.60	237.30	0.083	0.511	5.26	0.066	4.84	0.919	0.056	2.07	413
5D	0.016	19.33	4.53	169.45	0.027	0.704	7.32	0.087	6.45	0.881	0.059	3.47	537
6D	0.015	27.78	69.79	67.52	1.034	4.281	4.16	0.285	3.79	0.911	0.109	1.71	1616
9D	0.014	10.20	71.88	72.14	0.996	0.808	5.62	0.096	3.68	0.655	0.061	4.25	594

Table C: *(continued)*

PC44D					Isotope ratios								
Spot	***ƒ*** $_{206}$ ^{a}	**Pb**	**Th**	**U**	**Th/U**^{b}	^{207}**Pb**	**1 s [%]**	^{206}**Pb**	**1 s [%]**	**Rho**^{d}	^{207}**Pb**	**1 s [%]**	^{206}**Pb**

		ppm	ppm	ppm		^{235}U		^{238}U			^{206}Pb^{e}		^{238}U
1E	0.016	19.77	20.57	72.65	0.283	1.967	5.98	0.181	5.05	0.844	0.079	3.21	1072
2E	0.016	129.79	361.69	333.67	1.084	4.372	5.93	0.297	5.61	0.946	0.107	1.92	1679
3E	0.017	86.77	130.97	278.19	0.471	2.792	3.50	0.229	3.02	0.863	0.089	1.77	1327
4E	0.016	37.52	72.87	122.91	0.593	2.552	5.57	0.220	5.01	0.900	0.084	2.43	1279
6E	0.017	56.83	16.11	703.42	0.023	0.441	7.09	0.059	6.50	0.916	0.054	2.84	369
7E	0.016	38.32	74.91	164.51	0.455	1.696	8.96	0.168	8.14	0.908	0.073	3.75	999
8E	0.016	104.43	150.14	364.57	0.412	2.212	5.62	0.196	4.76	0.847	0.082	2.99	1151
1F	0.017	91.48	210.32	341.35	0.616	1.805	4.44	0.169	3.86	0.869	0.077	2.20	1008
2F	0.016	23.51	27.41	79.57	0.344	2.154	5.78	0.192	4.84	0.838	0.081	3.16	1132
3F	0.016	35.86	9.54	379.64	0.025	0.559	6.23	0.071	5.47	0.864	0.057	3.18	443
4F	0.015	30.84	60.16	65.62	0.917	4.950	5.12	0.307	3.57	0.697	0.117	3.67	1726
5F	0.016	27.75	42.25	257.89	0.164	0.689	6.81	0.085	5.35	0.786	0.059	4.21	523
6F	0.016	63.76	135.91	284.29	0.478	1.745	5.76	0.167	4.43	0.770	0.076	3.68	995
9F	0.017	125.86	59.74	476.76	0.125	1.767	4.42	0.171	3.86	0.874	0.075	2.15	1020
2G	0.016	46.26	19.40	607.43	0.032	0.427	8.43	0.057	7.40	0.878	0.054	4.04	356
3G	0.012	14.70	98.18	178.40	0.550	0.471	9.10	0.062	5.29	0.581	0.055	7.41	390
4G	0.016	26.32	35.68	263.00	0.136	0.539	7.01	0.070	4.88	0.697	0.056	5.02	438
5G	0.015	31.39	244.63	292.98	0.835	0.597	6.56	0.077	4.10	0.626	0.057	5.12	475
6G	0.017	102.42	90.01	377.18	0.239	2.112	3.38	0.194	2.38	0.703	0.079	2.41	1140
7G	0.016	49.10	9.64	624.75	0.015	0.436	6.24	0.059	4.92	0.789	0.054	3.83	368
1H	0.017	107.55	133.00	457.67	0.291	1.755	4.27	0.177	3.12	0.729	0.072	2.92	1051
2H	0.000	36.47	338.78	582.68	0.581	0.572	5.52	0.074	3.52	0.639	0.056	4.24	460
3H	0.017	83.03	149.77	327.35	0.458	1.605	3.56	0.162	2.18	0.613	0.072	2.82	971
4H	0.017	88.22	542.80	846.54	0.641	0.600	7.64	0.077	4.50	0.589	0.057	6.18	477
5H	0.017	16.80	25.54	66.75	0.383	1.582	6.96	0.159	3.94	0.566	0.072	5.74	949
7H	0.015	26.38	392.71	226.58	1.733	0.602	8.64	0.077	4.67	0.540	0.057	7.27	478
9H	0.017	146.58	241.85	399.21	0.606	2.661	5.93	0.225	5.30	0.893	0.086	2.66	1311

Table C: *(continued).*

PC44D					Isotope ratios								
Spot	***ƒ*** **206**[a]	**Pb**	**Th**	**U**	**Th/U**[b]	**^{207}Pb**	**1 s [%]**	**^{206}Pb**	**1 s [%]**	**Rho**[d]	**^{207}Pb**	**1 s [%]**	**^{206}P**
		ppm	**ppm**	**ppm**		**^{235}U**		**^{238}U**			**^{206}Pb^{e}**		**^{238}**
1I	0.017	16.79	28.25	55.42	0.510	2.738	7.67	0.222	4.05	0.528	0.089	6.51	129
2I	0.017	12.61	63.36	116.27	0.545	0.622	9.87	0.079	4.44	0.450	0.057	8.81	488
3I	0.017	86.64	146.05	241.10	0.606	3.028	3.80	0.245	2.70	0.711	0.090	2.67	141
4I	0.017	44.41	236.56	399.05	0.593	0.606	6.82	0.077	4.31	0.632	0.057	5.29	478
6I	0.017	24.47	48.35	99.98	0.484	1.705	8.31	0.170	6.37	0.766	0.073	5.34	100

8I	0.017	18.33	49.64	176.85	0.281	0.603	8.50	0.077	4.51	0.530	0.057	7.20	477
9I	0.016	19.72	166.60	175.50	0.949	0.543	7.52	0.071	5.13	0.682	0.056	5.50	440
1J	0.016	41.75	11.88	570.10	0.021	0.430	6.61	0.058	4.84	0.733	0.054	4.49	361
2J	0.014	22.32	225.56	211.44	1.067	0.580	6.45	0.074	4.50	0.697	0.057	4.63	463
3J	0.015	27.50	134.66	276.76	0.487	0.555	6.58	0.071	4.49	0.682	0.057	4.81	442
5J	0.015	35.75	217.70	362.06	0.601	0.545	6.40	0.071	4.00	0.625	0.056	5.00	441
7J	0.017	134.81	22.92	602.83	0.038	1.892	3.78	0.175	1.76	0.465	0.078	3.34	104
9J	0.013	16.40	98.88	146.00	0.677	0.639	7.56	0.081	3.92	0.519	0.057	6.46	501
2K	0.015	57.47	510.49	494.29	1.033	0.611	5.44	0.077	4.09	0.752	0.057	3.58	480
5K	0.011	9.61	85.64	91.71	0.934	0.580	12.56	0.075	5.53	0.440	0.056	11.28	465
8K	0.016	33.01	15.92	436.63	0.036	0.446	6.14	0.059	4.33	0.704	0.055	4.36	369
9K	0.015	74.26	279.17	192.32	1.452	2.918	4.22	0.237	3.32	0.787	0.089	2.61	137
2L	0.017	81.60	5.19	318.19	0.016	2.129	3.93	0.195	2.85	0.716	0.079	2.78	114
3L	0.016	48.09	117.62	194.03	0.606	1.832	6.36	0.178	3.47	0.545	0.075	5.33	105
6L	0.017	9.32	15.42	39.13	0.394	1.773	9.80	0.177	3.05	0.311	0.073	9.31	105
7L	0.017	80.80	215.84	607.85	0.355	0.811	7.24	0.096	5.34	0.737	0.061	4.89	593
8L	0.017	9.21	16.76	37.64	0.445	1.367	11.42	0.142	5.81	0.509	0.070	9.83	854
9L	0.016	29.18	195.70	269.05	0.727	0.589	9.17	0.075	4.82	0.525	0.057	7.81	467

Table C: *(continued).*

PC44D					Isotope ratios								
Spot	f_{206} [a]	**Pb** ppm	**Th** ppm	**U** ppm	**Th/U** [b]	^{207}Pb/^{235}U	**1 s [%]**	^{206}Pb/^{238}U	**1 s [%]**	**Rho** [d]	^{207}Pb/^{206}Pb [e]	**1 s [%]**	^{206}P… / ^{238}…
1M	0.017	43.04	208.34	324.48	0.642	1.038	6.02	0.116	4.92	0.818	0.065	3.46	70
3M	0.017	31.92	40.78	244.44	0.167	1.364	7.20	0.142	6.18	0.859	0.070	3.69	85
6M	0.017	44.23	411.37	536.99	0.766	0.534	8.79	0.069	7.84	0.891	0.056	3.99	42
7M	0.016	42.43	356.46	532.51	0.669	0.571	8.48	0.072	7.33	0.864	0.057	4.26	45
8M	0.016	29.08	245.25	355.99	0.689	0.559	9.66	0.071	8.39	0.868	0.057	4.79	44
2N	0.016	63.99	282.41	417.68	0.676	0.840	13.65	0.099	10.96	0.803	0.062	8.14	60
4N	0.016	26.62	86.85	246.42	0.352	0.675	13.74	0.083	11.81	0.860	0.059	7.02	51
5N	0.017	54.74	61.63	153.52	0.401	2.798	8.08	0.223	5.90	0.731	0.091	5.52	129
8N	0.016	164.36	153.35	204.29	0.751	12.318	6.04	0.483	5.59	0.925	0.185	2.29	254
1O	0.015	70.47	168.04	100.30	1.675	11.437	5.55	0.466	4.64	0.836	0.178	3.04	246
2O	0.017	50.15	182.17	601.98	0.303	0.585	11.89	0.075	10.02	0.842	0.057	6.41	46
3O	0.016	37.32	103.67	210.56	0.492	2.112	7.21	0.193	4.34	0.602	0.079	5.76	114
4O	0.016	21.27	67.95	90.23	0.753	2.064	9.34	0.189	7.48	0.801	0.079	5.59	111
5O	0.017	30.55	75.22	138.16	0.544	1.921	7.02	0.184	4.94	0.703	0.076	4.99	108

6O	0.017	20.90	39.71	70.26	0.565	3.008	7.60	0.242	5.38	0.707	0.090	5.37	139
7O	0.017	37.82	88.14	158.74	0.555	2.166	6.99	0.195	4.85	0.694	0.081	5.03	114
8O	0.017	20.19	117.82	225.33	0.523	0.598	11.66	0.076	9.64	0.827	0.057	6.56	47
9O	0.017	54.17	272.67	597.01	0.457	0.572	11.72	0.074	9.98	0.852	0.056	6.15	45

Declaration of interests

☐
√ The authors declare that they have no known competing financial interests or personal relationships that could have appeared to influence the work reported in this paper.

☐ The authors declare the following financial interests/personal relationships which may be considered as potential competing interests:

- Geodynamic evolution of the western North Patagonian basement presents five stages.
- After the Carboniferous sedimentation started the first tectonic metamorphic stage.
- The peak metamorphic stage is linked to the Permian magmatism.
- The second and third deformational stages correspond to the uplift path of the basement.
- The subduction setting prevails during the evolution of the late Paleozoic basement.

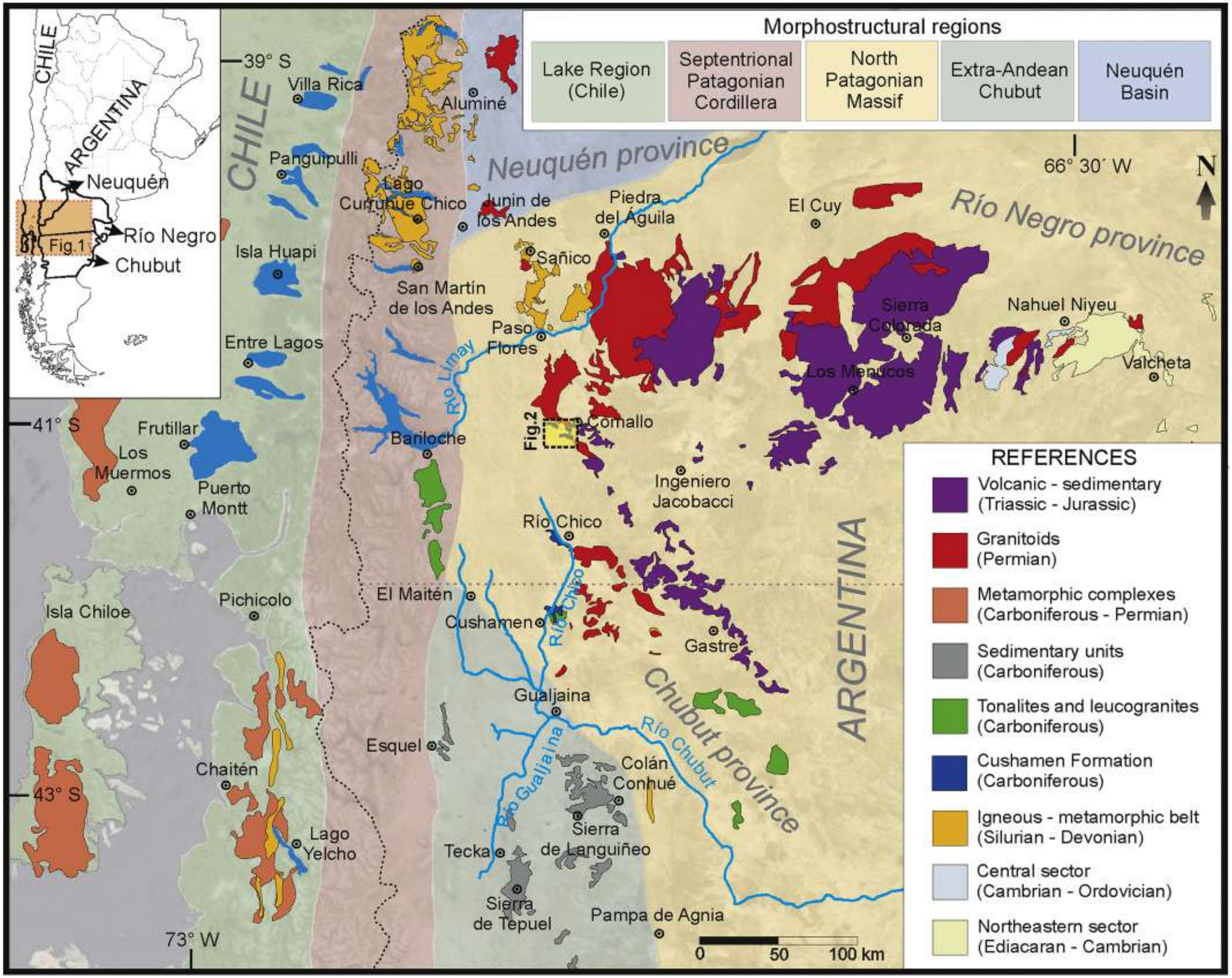

Morphostructural regions
Lake Region (Chile)
Septentrional Patagonian Cordillera
North Patagonian Massif
Extra-Andean Chubut
Neuquén Basin
CHILE
ARGENTINA
Neuquén
Río Negro
Chubut
Fig.1
39° S
41° S
43° S
73° W
66° 30´ W
N
Villa Rica
Aluminé
Panguipulli
Lago Curruhue Chico
Junín de los Andes
Isla Huapi
San Martín de los Andes
Entre Lagos
Frutillar
Los Muermos
Puerto Montt
Bariloche
Neuquén province
Río Negro province
Chubut province
Piedra del Águila
El Cuy
Sañico
Paso Flores
Río Limay
Sierra Colorada
Los Menucos
Nahuel Niyeu
Valcheta
Comallo
Fig.2
Ingeniero Jacobacci
Río Chico
El Maitén
Cushamen
Gastre
Isla Chiloe
Pichicolo
Gualjaina
Río Chubut
Río Gualjaina
Esquel
Chaitén
Colán Conhué
Sierra de Languiñeo
Lago Yelcho
Tecka
Sierra de Tepuel
Pampa de Agnia
0 50 100 km
REFERENCES
Volcanic - sedimentary (Triassic - Jurassic)
Granitoids (Permian)
Metamorphic complexes (Carboniferous - Permian)
Sedimentary units (Carboniferous)
Tonalites and leucogranites (Carboniferous)
Cushamen Formation (Carboniferous)
Igneous - metamorphic belt (Silurian - Devonian)
Central sector (Cambrian - Ordovician)
Northeastern sector (Ediacaran - Cambrian)

Figure 1

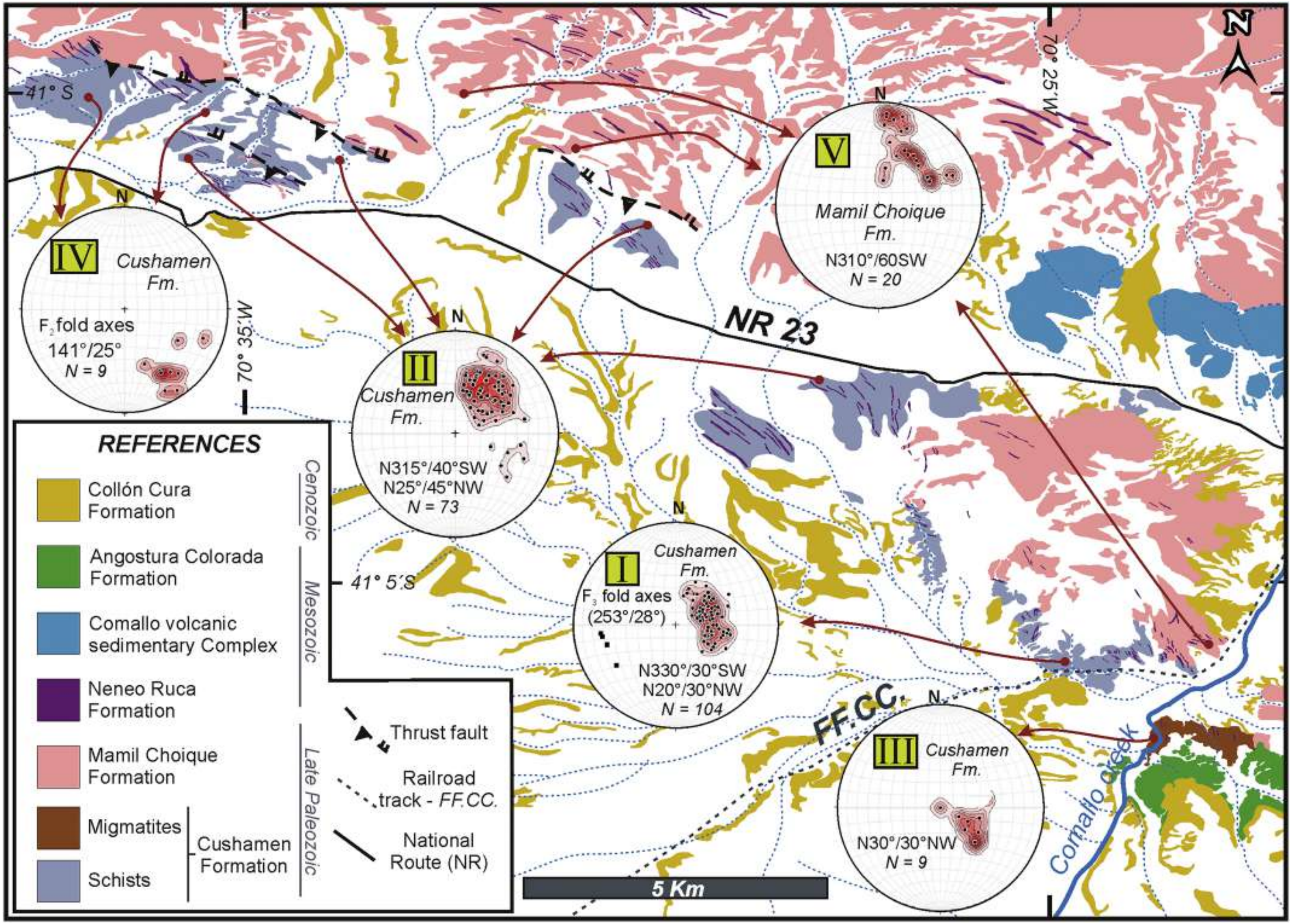

41° S
70° 25'W
70° 35'W
41° 5'S
N
V
Mamil Choique Fm.
N310°/60SW
N = 20
IV
Cushamen Fm.
F2 fold axes
141°/25°
N = 9
II
Cushamen Fm.
N315°/40°SW
N25°/45°NW
N = 73
I
Cushamen Fm.
F3 fold axes
(253°/28°)
N330°/30°SW
N20°/30°NW
N = 104
III
Cushamen Fm.
N30°/30°NW
N = 9
NR 23
FF.CC.
Comallo creek
5 Km
REFERENCES
Collón Cura Formation
Angostura Colorada Formation
Comallo volcanic sedimentary Complex
Neneo Ruca Formation
Mamil Choique Formation
Migmatites
Schists
Cushamen Formation
Cenozoic
Mesozoic
Late Paleozoic
Thrust fault
Railroad track - FF.CC.
National Route (NR)

Figure 2

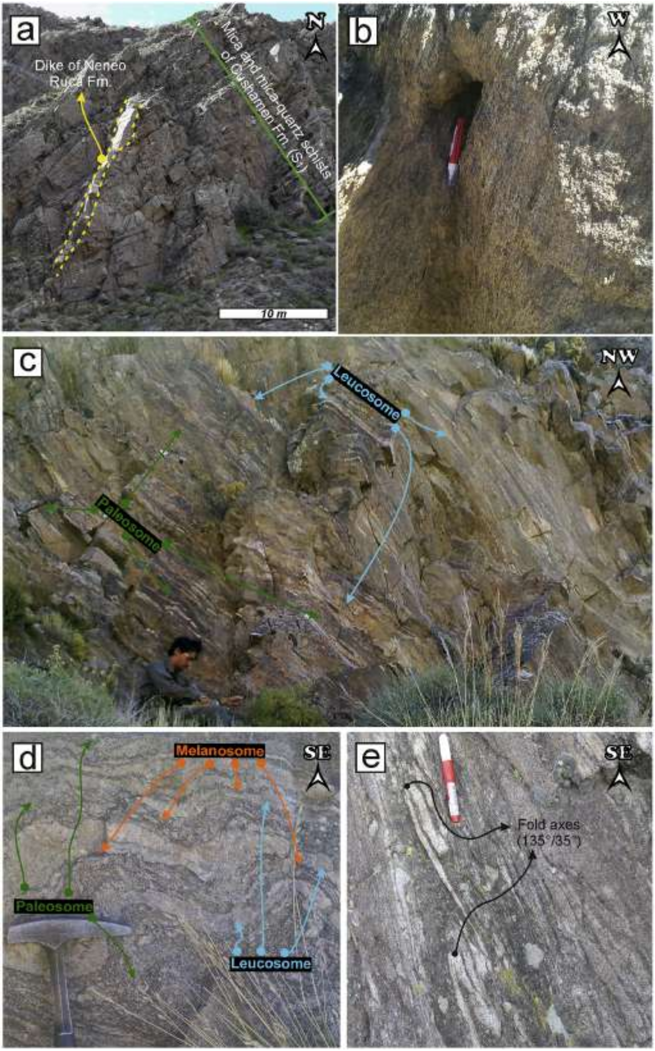
a
N
Dike of Neneo Ruca Fm.
Mica and mica-quartz schists of Cushamen Fm. (S1)
10 m
b
W
c
NW
Leucosome
Paleosome
d
SE
Melanosome
Paleosome
Leucosome
e
SE
Fold axes (135°/35°)

Figure 3

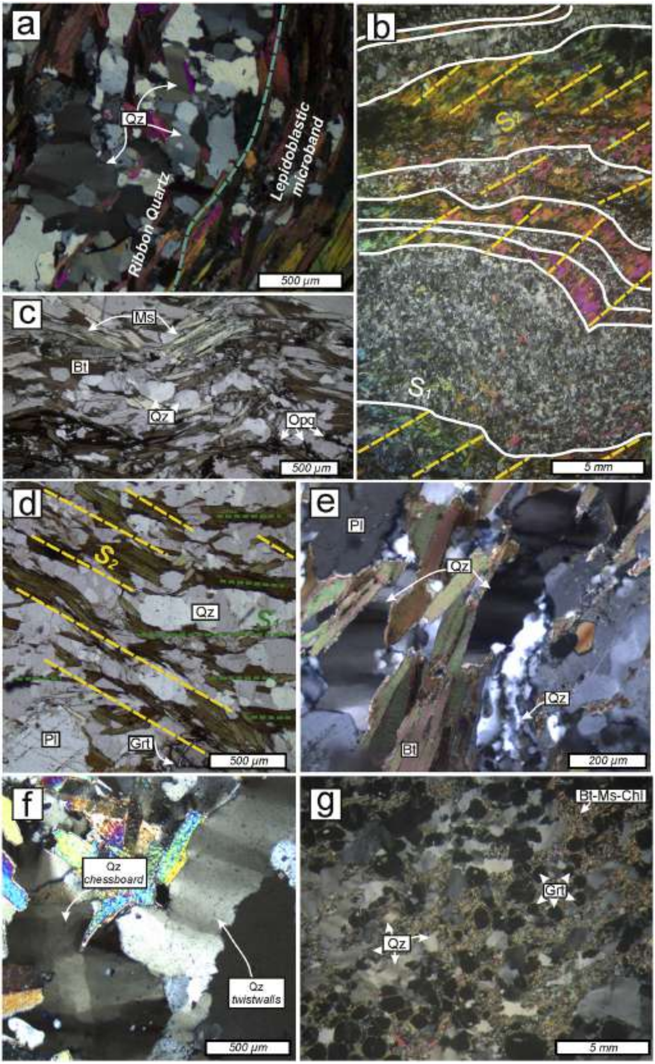
a
Qz
Ribbon Quartz
Lepidoblastic microband
500 µm
b
S2
S1
5 mm
c
Ms
Bt
Qz
Opq
500 µm
d
S2
Qz
S1
Pl
Grt
500 µm
e
Pl
Qz
Qz
Bt
200 µm
f
Qz chessboard
Qz twistwalls
500 µm
g
Bt-Ms-Chl
Grt
Qz
5 mm

Figure 4

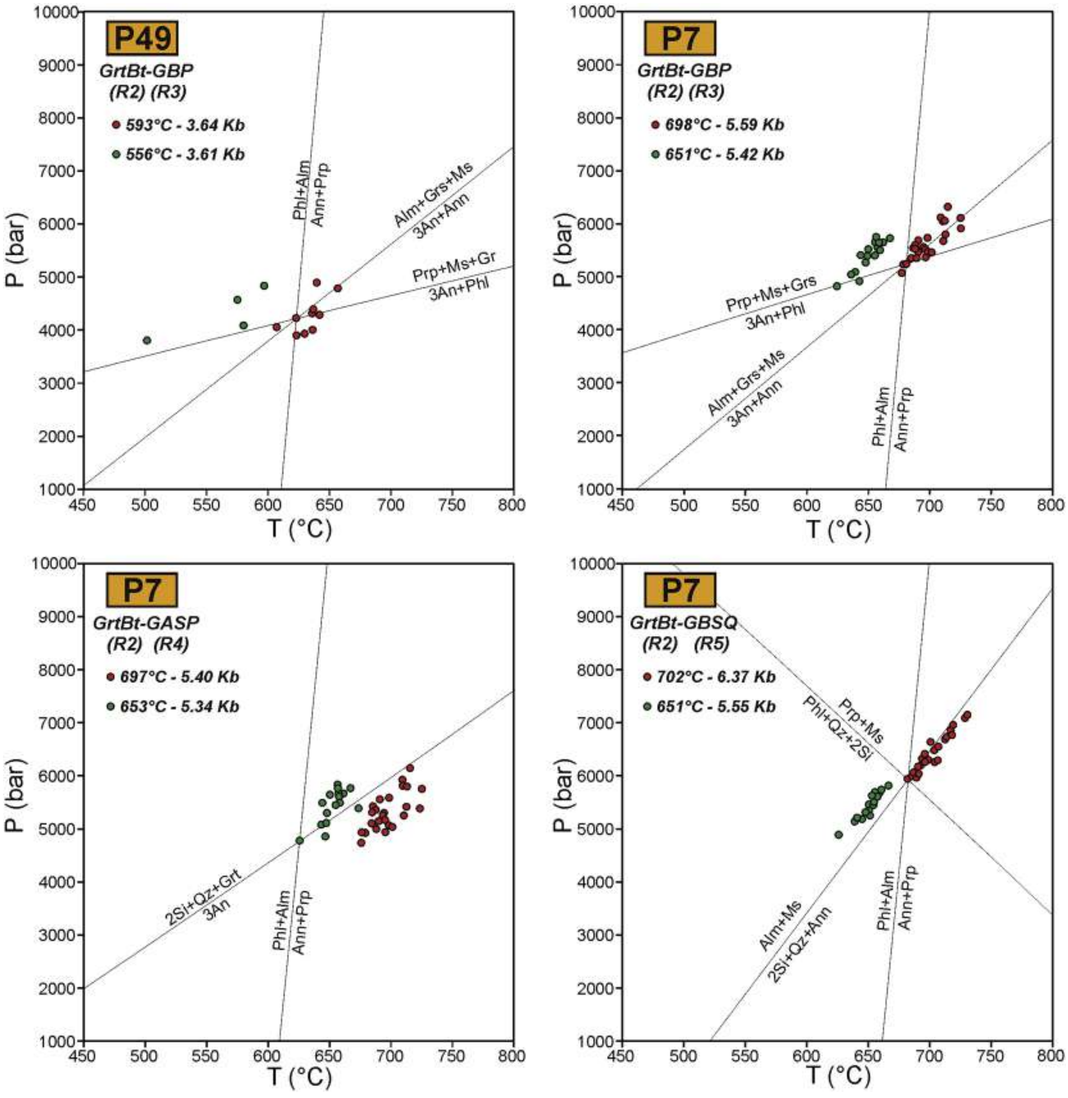
P49
GrtBt-GBP
(R2) (R3)
593°C - 3.64 Kb
556°C - 3.61 Kb
Phl+Alm
Ann+Prp
Alm+Grs+Ms
3An+Ann
Prp+Ms+Gr
3An+Phl
P (bar)
T (°C)
P7
GrtBt-GBP
(R2) (R3)
698°C - 5.59 Kb
651°C - 5.42 Kb
Prp+Ms+Grs
3An+Phl
Alm+Grs+Ms
3An+Ann
Phl+Alm
Ann+Prp
P7
GrtBt-GASP
(R2) (R4)
697°C - 5.40 Kb
653°C - 5.34 Kb
2Si+Qz+Grt
3An
Phl+Alm
Ann+Prp
P7
GrtBt-GBSQ
(R2) (R5)
702°C - 6.37 Kb
651°C - 5.55 Kb
Prp+Ms
Phl+Qz+2Si
Alm+Ms
2Si+Qz+Ann
Phl+Alm
Ann+Prp

Figure 5

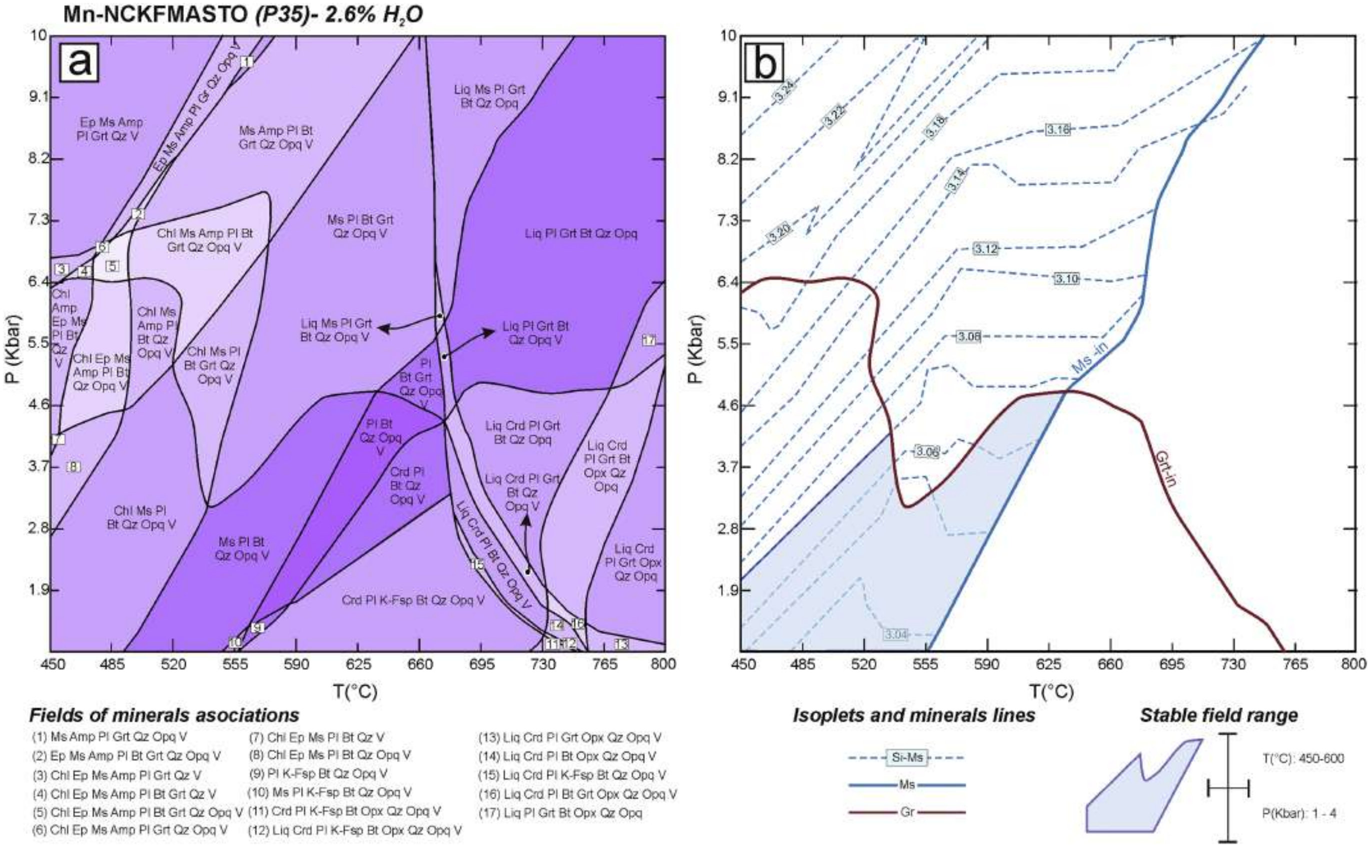
Mn-NCKFMASTO (P35)- 2.6% H2O
a
b
P (Kbar)
T(°C)
Ep Ms Amp Pl Grt Qz V
Ep Ms Amp Pl Gr Qz Opq V
Ms Amp Pl Bt Grt Qz Opq V
Liq Ms Pl Grt Bt Qz Opq
Chl Ms Amp Pl Bt Grt Qz Opq V
Ms Pl Bt Grt Qz Opq V
Liq Pl Grt Bt Qz Opq
Chl Amp Ep Ms Pl Bt Qz V
Chl Ms Amp Pl Bt Qz Opq V
Chl Ep Ms Amp Pl Bt Qz Opq V
Chl Ms Pl Bt Grt Qz Opq V
Liq Ms Pl Grt Bt Qz Opq V
Liq Pl Grt Bt Qz Opq V
Pl Bt Grt Qz Opq V
Pl Bt Qz Opq V
Liq Crd Pl Grt Bt Qz Opq
Crd Pl Bt Qz Opq V
Liq Crd Pl Grt Bt Qz Opq V
Liq Crd Pl Grt Bt Opx Qz Opq
Chl Ms Pl Bt Qz Opq V
Ms Pl Bt Qz Opq V
Liq Crd Pl Bt Qz Opq V
Liq Crd Pl Grt Opx Qz Opq
Crd Pl K-Fsp Bt Qz Opq V
Fields of minerals asociations
(1) Ms Amp Pl Grt Qz Opq V
(2) Ep Ms Amp Pl Bt Grt Qz Opq V
(3) Chl Ep Ms Amp Pl Grt Qz V
(4) Chl Ep Ms Amp Pl Bt Grt Qz V
(5) Chl Ep Ms Amp Pl Bt Grt Qz Opq V
(6) Chl Ep Ms Amp Pl Grt Qz Opq V
(7) Chl Ep Ms Pl Bt Qz V
(8) Chl Ep Ms Pl Bt Qz Opq V
(9) Pl K-Fsp Bt Qz Opq V
(10) Ms Pl K-Fsp Bt Qz Opq V
(11) Crd Pl K-Fsp Bt Opx Qz Opq V
(12) Liq Crd Pl K-Fsp Bt Opx Qz Opq V
(13) Liq Crd Pl Grt Opx Qz Opq V
(14) Liq Crd Pl Bt Opx Qz Opq V
(15) Liq Crd Pl K-Fsp Bt Qz Opq V
(16) Liq Crd Pl Bt Grt Opx Qz Opq V
(17) Liq Pl Grt Bt Opx Qz Opq
Ms -in
Grt-in
Isoplets and minerals lines
Si-Ms
Ms
Gr
Stable field range
T(°C): 450-600
P(Kbar): 1 - 4

Figure 6

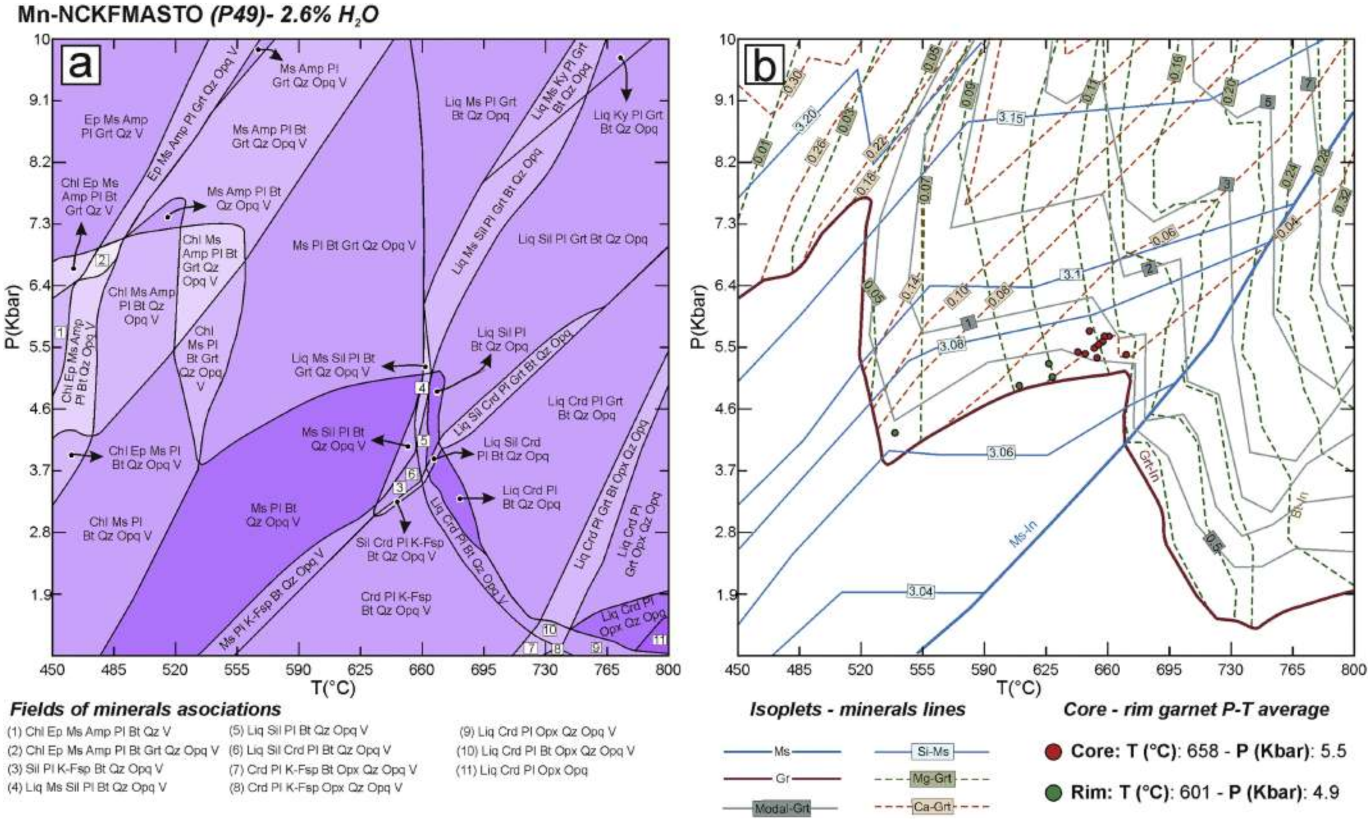

Mn-NCKFMASTO (P49)- 2.6% H2O
a
b
P(Kbar)
T(°C)
Ep Ms Amp Pl Grt Qz V
Chl Ep Ms Amp Pl Bt Grt Qz V
Ms Amp Pl Grt Qz Opq V
Ms Amp Pl Bt Grt Qz Opq V
Ms Amp Pl Bt Qz Opq V
Chl Ms Amp Pl Bt Grt Qz Opq V
Chl Ms Amp Pl Bt Qz Opq V
Chl Ms Pl Bt Grt Qz Opq V
Chl Ep Ms Pl Bt Qz Opq V
Chl Ms Pl Bt Qz Opq V
Ms Pl Bt Grt Qz Opq V
Liq Ms Pl Grt Bt Qz Opq
Liq Ms Ky Pl Grt Bt Qz Opq
Liq Ky Pl Grt Bt Qz Opq
Liq Ms Sil Pl Grt Bt Qz Opq
Liq Sil Pl Grt Bt Qz Opq
Liq Ms Sil Pl Bt Grt Qz Opq V
Liq Sil Pl Bt Qz Opq
Liq Sil Crd Pl Grt Bt Qz Opq
Liq Crd Pl Grt Bt Qz Opq
Ms Sil Pl Bt Qz Opq V
Liq Sil Crd Pl Bt Qz Opq
Liq Crd Pl Bt Qz Opq
Ms Pl Bt Qz Opq V
Sil Crd Pl K-Fsp Bt Qz Opq V
Liq Crd Pl Bt Qz Opq V
Liq Crd Pl Grt Bt Opx Qz Opq
Liq Crd Pl Grt Opx Qz Opq
Ms Pl K-Fsp Bt Qz Opq V
Crd Pl K-Fsp Bt Qz Opq V
Liq Crd Pl Opx Qz Opq
Ms-In
Grt-In
Bt-In
Fields of minerals asociations
(1) Chl Ep Ms Amp Pl Bt Qz V
(2) Chl Ep Ms Amp Pl Bt Grt Qz Opq V
(3) Sil Pl K-Fsp Bt Qz Opq V
(4) Liq Ms Sil Pl Bt Qz Opq V
(5) Liq Sil Pl Bt Qz Opq V
(6) Liq Sil Crd Pl Bt Qz Opq V
(7) Crd Pl K-Fsp Bt Opx Qz Opq V
(8) Crd Pl K-Fsp Opx Qz Opq V
(9) Liq Crd Pl Opx Qz Opq V
(10) Liq Crd Pl Bt Opx Qz Opq V
(11) Liq Crd Pl Opx Opq
Isoplets - minerals lines
Ms
Gr
Modal-Grt
Si-Ms
Mg-Grt
Ca-Grt
Core - rim garnet P-T average
Core: T (°C): 658 - P (Kbar): 5.5
Rim: T (°C): 601 - P (Kbar): 4.9

Figure 7

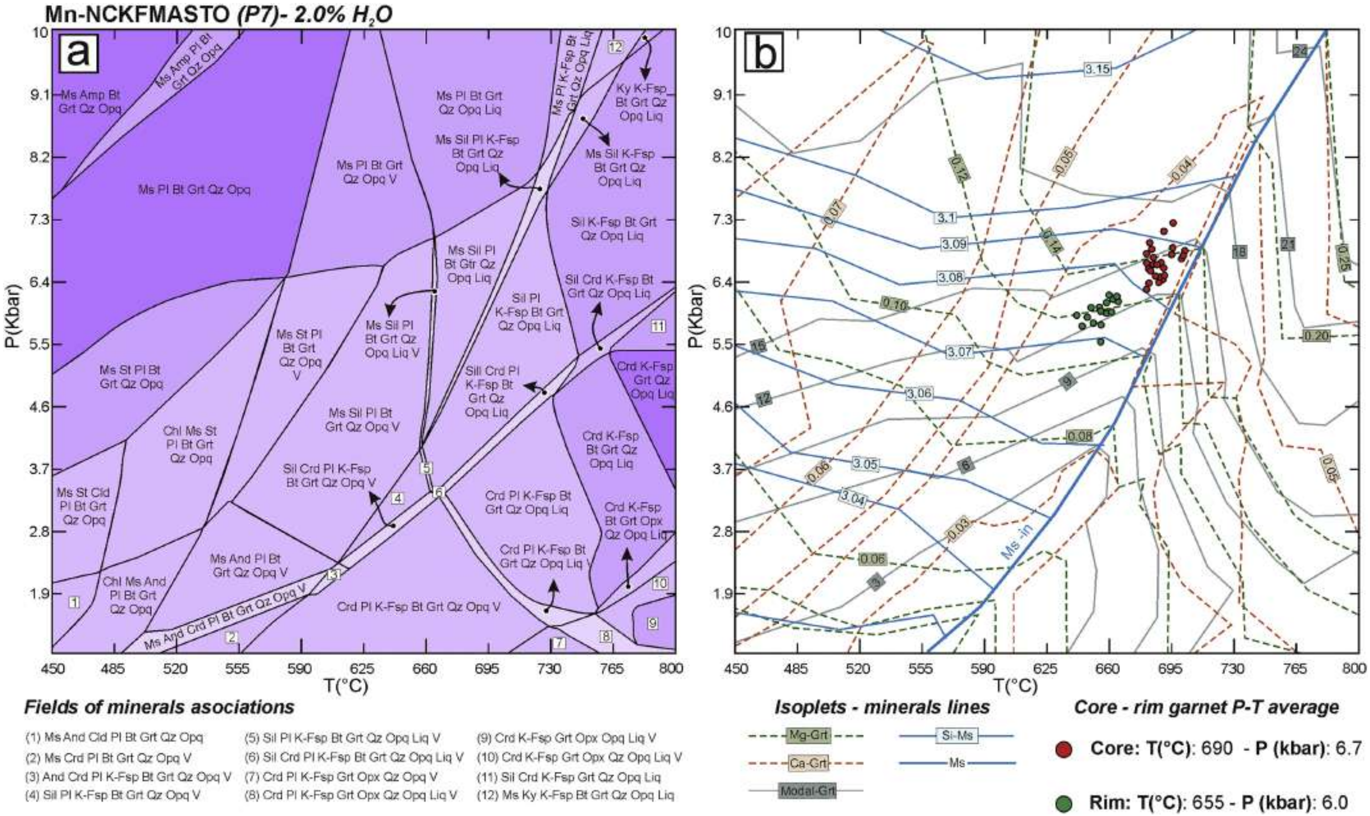

Mn-NCKFMASTO (P7)- 2.0% H_2O
a
b
P(Kbar)
T(°C)
Ms Amp Bt Grt Qz Opq
Ms Amp Pl Bt Grt Qz Opq
Ms Pl Bt Grt Qz Opq
Ms Pl Bt Grt Qz Opq V
Ms Pl Bt Grt Qz Opq Liq
Ms Sil Pl K-Fsp Bt Grt Qz Opq Liq
Ms Pl K-Fsp Bt Grt Qz Opq Liq
Ky K-Fsp Bt Grt Qz Opq Liq
Ms Sil K-Fsp Bt Grt Qz Opq Liq
Sil K-Fsp Bt Grt Qz Opq Liq
Sil Crd K-Fsp Bt Grt Qz Opq Liq
Ms Sil Pl Bt Gtr Qz Opq Liq
Sil Pl K-Fsp Bt Grt Qz Opq Liq
Ms Sil Pl Bt Grt Qz Opq Liq V
Ms St Pl Bt Grt Qz Opq V
Ms St Pl Bt Grt Qz Opq
Sill Crd Pl K-Fsp Bt Grt Qz Opq Liq
Crd K-Fsp Grt Qz Opq Liq
Ms Sil Pl Bt Grt Qz Opq V
Chl Ms St Pl Bt Grt Qz Opq
Crd K-Fsp Bt Grt Qz Opq Liq
Sil Crd Pl K-Fsp Bt Grt Qz Opq V
Ms St Cld Pl Bt Grt Qz Opq
Crd Pl K-Fsp Bt Grt Qz Opq Liq
Crd K-Fsp Bt Grt Opx Qz Opq Liq
Ms And Pl Bt Grt Qz Opq V
Chl Ms And Pl Bt Grt Qz Opq
Crd Pl K-Fsp Bt Grt Qz Opq Liq V
Ms And Crd Pl Bt Grt Qz Opq V
Crd Pl K-Fsp Bt Grt Qz Opq V
Ms -in
Fields of minerals asociations
(1) Ms And Cld Pl Bt Grt Qz Opq
(2) Ms Crd Pl Bt Grt Qz Opq V
(3) And Crd Pl K-Fsp Bt Grt Qz Opq V
(4) Sil Pl K-Fsp Bt Grt Qz Opq V
(5) Sil Pl K-Fsp Bt Grt Qz Opq Liq V
(6) Sil Crd Pl K-Fsp Bt Grt Qz Opq Liq V
(7) Crd Pl K-Fsp Grt Opx Qz Opq V
(8) Crd Pl K-Fsp Grt Opx Qz Opq Liq V
(9) Crd K-Fsp Grt Opx Opq Liq V
(10) Crd K-Fsp Grt Opx Qz Opq Liq V
(11) Sil Crd K-Fsp Grt Qz Opq Liq
(12) Ms Ky K-Fsp Bt Grt Qz Opq Liq
Isoplets - minerals lines
Mg-Grt
Ca-Grt
Modal-Grt
Si-Ms
Ms
Core - rim garnet P-T average
Core: T(°C): 690 - P (kbar): 6.7
Rim: T(°C): 655 - P (kbar): 6.0

Figure 8

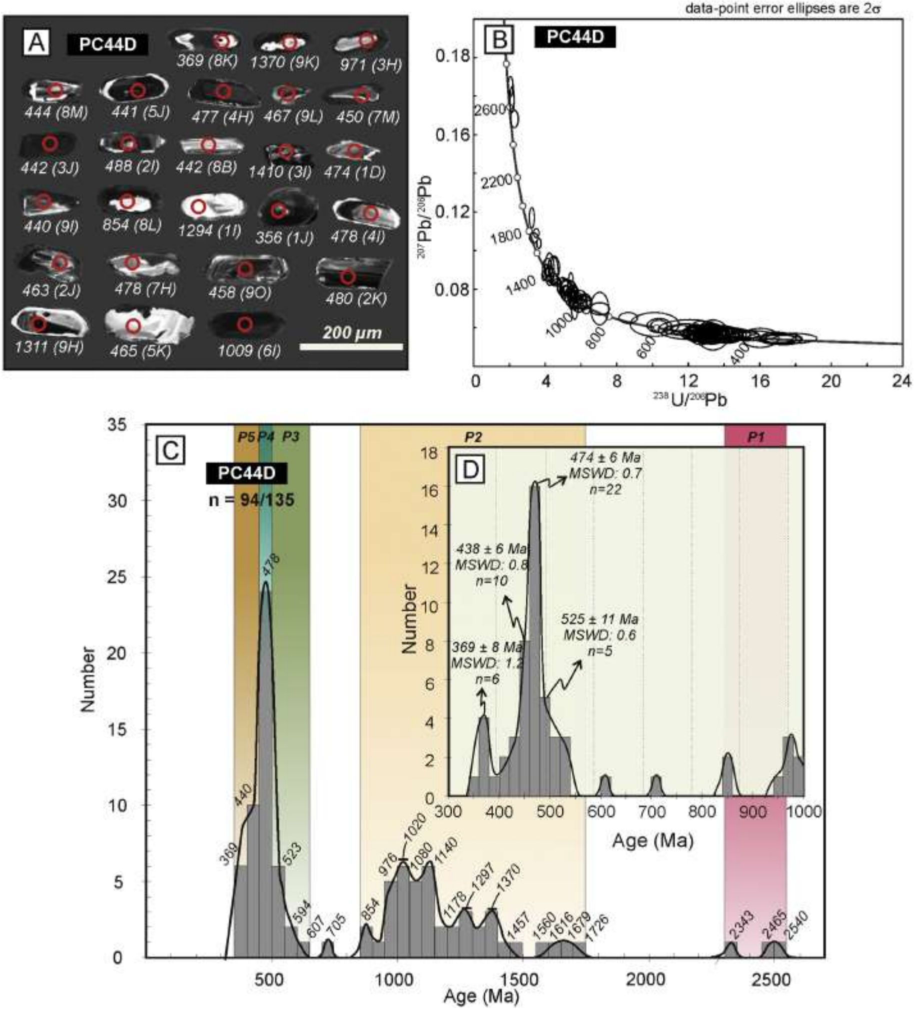

A
PC44D
369 (8K)
1370 (9K)
971 (3H)
444 (8M)
441 (5J)
477 (4H)
467 (9L)
450 (7M)
442 (3J)
488 (2I)
442 (8B)
1410 (3I)
474 (1D)
440 (9I)
854 (6L)
1294 (1I)
356 (1J)
478 (4I)
463 (2J)
478 (7H)
458 (9O)
480 (2K)
1311 (9H)
465 (5K)
1009 (6I)
200 µm
data-point error ellipses are 2σ
B
PC44D
$^{207}Pb/^{206}Pb$
$^{238}U/^{206}Pb$
C
PC44D
n = 94/135
P5 P4 P3
P2
P1
Number
Age (Ma)
D
474 ± 6 Ma
MSWD: 0.7
n=22
438 ± 6 Ma
MSWD: 0.8
n=10
525 ± 11 Ma
MSWD: 0.6
n=5
369 ± 8 Ma
MSWD: 1.2
n=6
Number
Age (Ma)

Figure 9

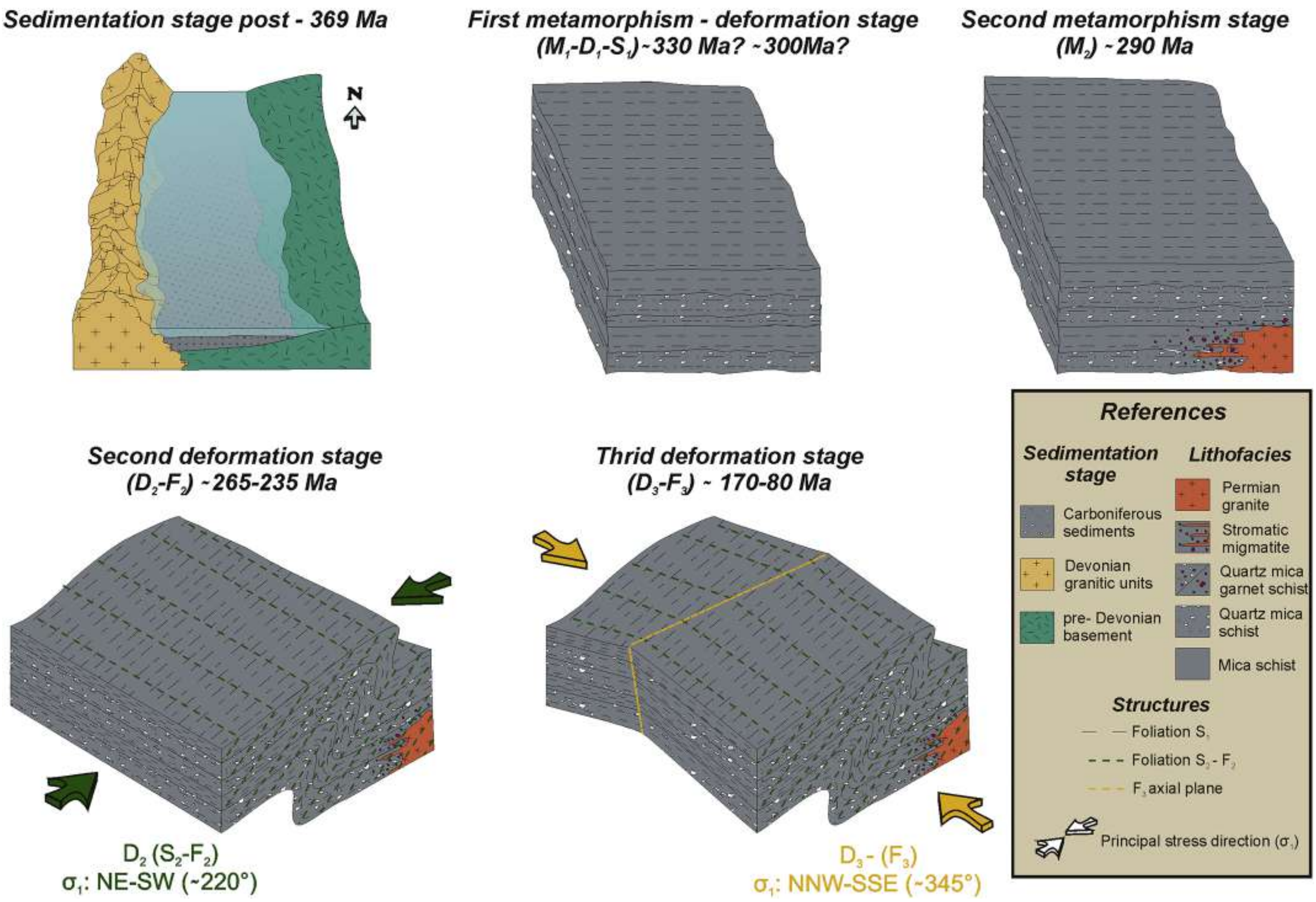

Sedimentation stage post - 369 Ma
First metamorphism - deformation stage
(M1-D1-S1)~330 Ma? ~300Ma?
Second metamorphism stage
(M2) ~290 Ma
N
Second deformation stage
(D2-F2) ~265-235 Ma
Thrid deformation stage
(D3-F3) ~ 170-80 Ma
D2 (S2-F2)
σ1: NE-SW (~220°)
D3- (F3)
σ1: NNW-SSE (~345°)
References
Sedimentation stage
Carboniferous sediments
Devonian granitic units
pre- Devonian basement
Lithofacies
Permian granite
Stromatic migmatite
Quartz mica garnet schist
Quartz mica schist
Mica schist
Structures
Foliation S1
Foliation S2 - F2
F3 axial plane
Principal stress direction (σ1)

Figure 10

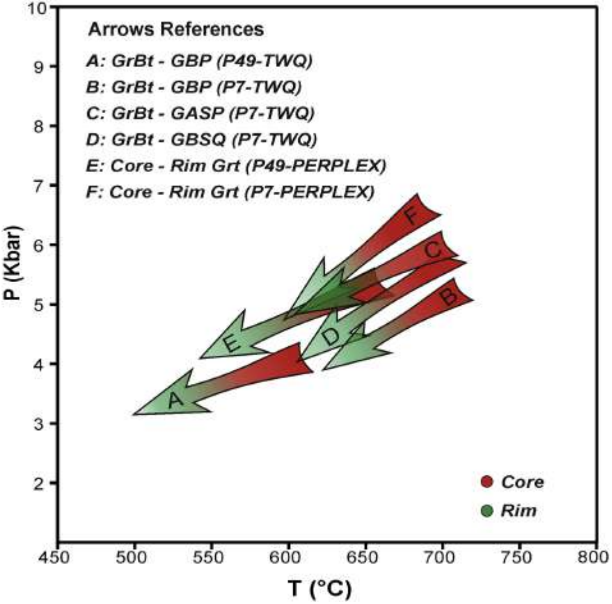
Arrows References
A: GrBt - GBP (P49-TWQ)
B: GrBt - GBP (P7-TWQ)
C: GrBt - GASP (P7-TWQ)
D: GrBt - GBSQ (P7-TWQ)
E: Core - Rim Grt (P49-PERPLEX)
F: Core - Rim Grt (P7-PERPLEX)
A
B
C
D
E
F
Core
Rim
P (Kbar)
T (°C)
10
9
8
7
6
5
4
3
2
450
500
550
600
650
700
750
800

Figure 11

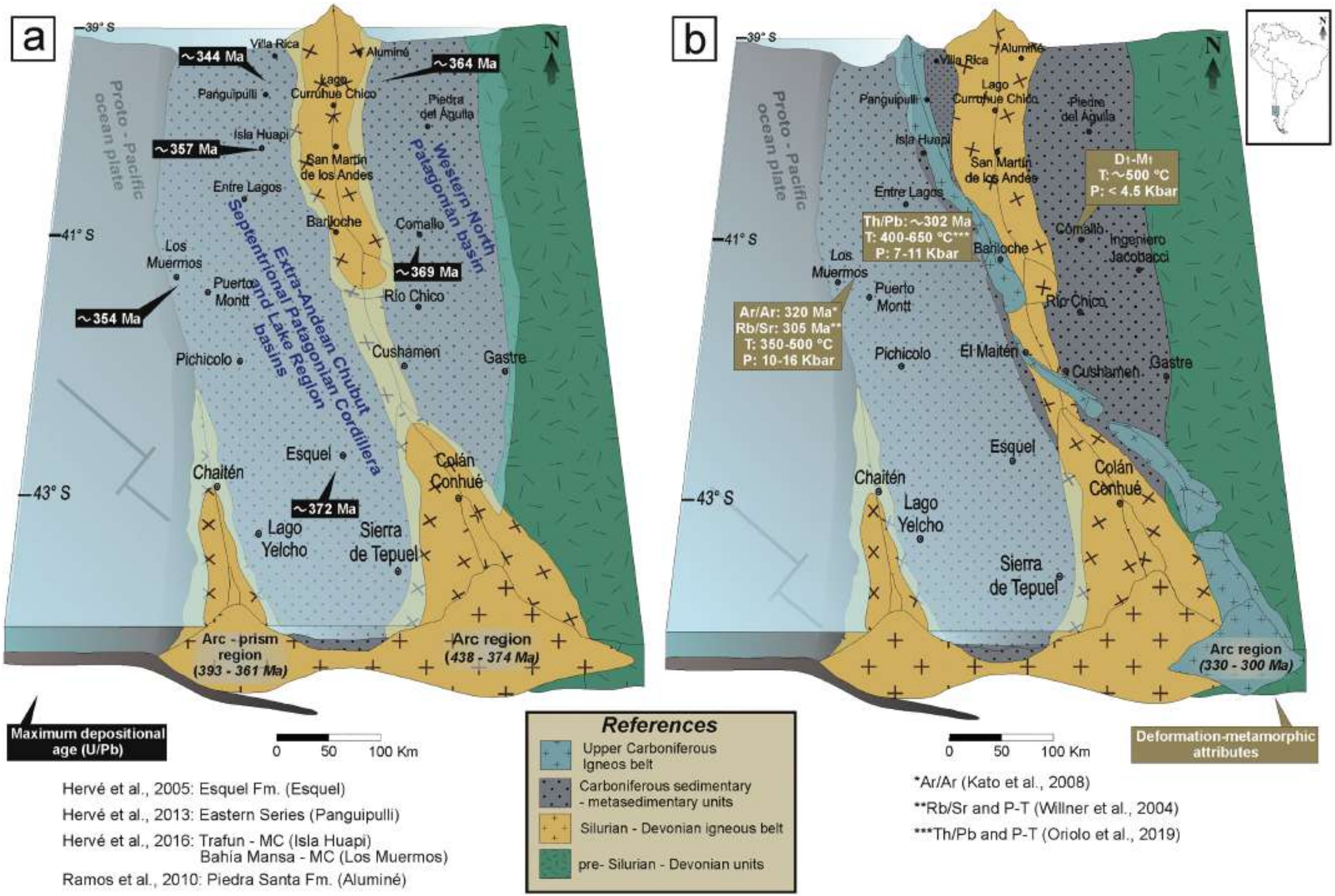
a
b
39° S
41° S
43° S
N
Villa Rica
Aluminé
Lago Curruhue Chico
Panguipulli
Piedra del Águila
Isla Huapi
San Martín de los Andes
Entre Lagos
Bariloche
Comallo
Los Muermos
Puerto Montt
Río Chico
Pichicolo
Cushamen
Gastre
Esquel
Chaitén
Colán Conhué
Lago Yelcho
Sierra de Tepuel
El Maitén
Ingeniero Jacobacci
Proto - Pacific ocean plate
Extra-Andean Chubut Septentrional Patagonian Cordillera and Lake Region basins
Western North Patagonian basin
~344 Ma
~364 Ma
~357 Ma
~369 Ma
~354 Ma
~372 Ma
Arc - prism region (393 - 361 Ma)
Arc region (438 - 374 Ma)
Arc region (330 - 300 Ma)
D1-M1
T: ~500 °C
P: < 4.5 Kbar
Th/Pb: ~302 Ma
T: 400-650 °C***
P: 7-11 Kbar
Ar/Ar: 320 Ma*
Rb/Sr: 305 Ma**
T: 350-500 °C
P: 10-16 Kbar
Maximum depositional age (U/Pb)
Deformation-metamorphic attributes
0 50 100 Km
References
Upper Carboniferous Igneos belt
Carboniferous sedimentary - metasedimentary units
Silurian - Devonian igneous belt
pre- Silurian - Devonian units
Hervé et al., 2005: Esquel Fm. (Esquel)
Hervé et al., 2013: Eastern Series (Panguipulli)
Hervé et al., 2016: Trafun - MC (Isla Huapi)
Bahía Mansa - MC (Los Muermos)
Ramos et al., 2010: Piedra Santa Fm. (Aluminé)
*Ar/Ar (Kato et al., 2008)
**Rb/Sr and P-T (Willner et al., 2004)
***Th/Pb and P-T (Oriolo et al., 2019)

Figure 12

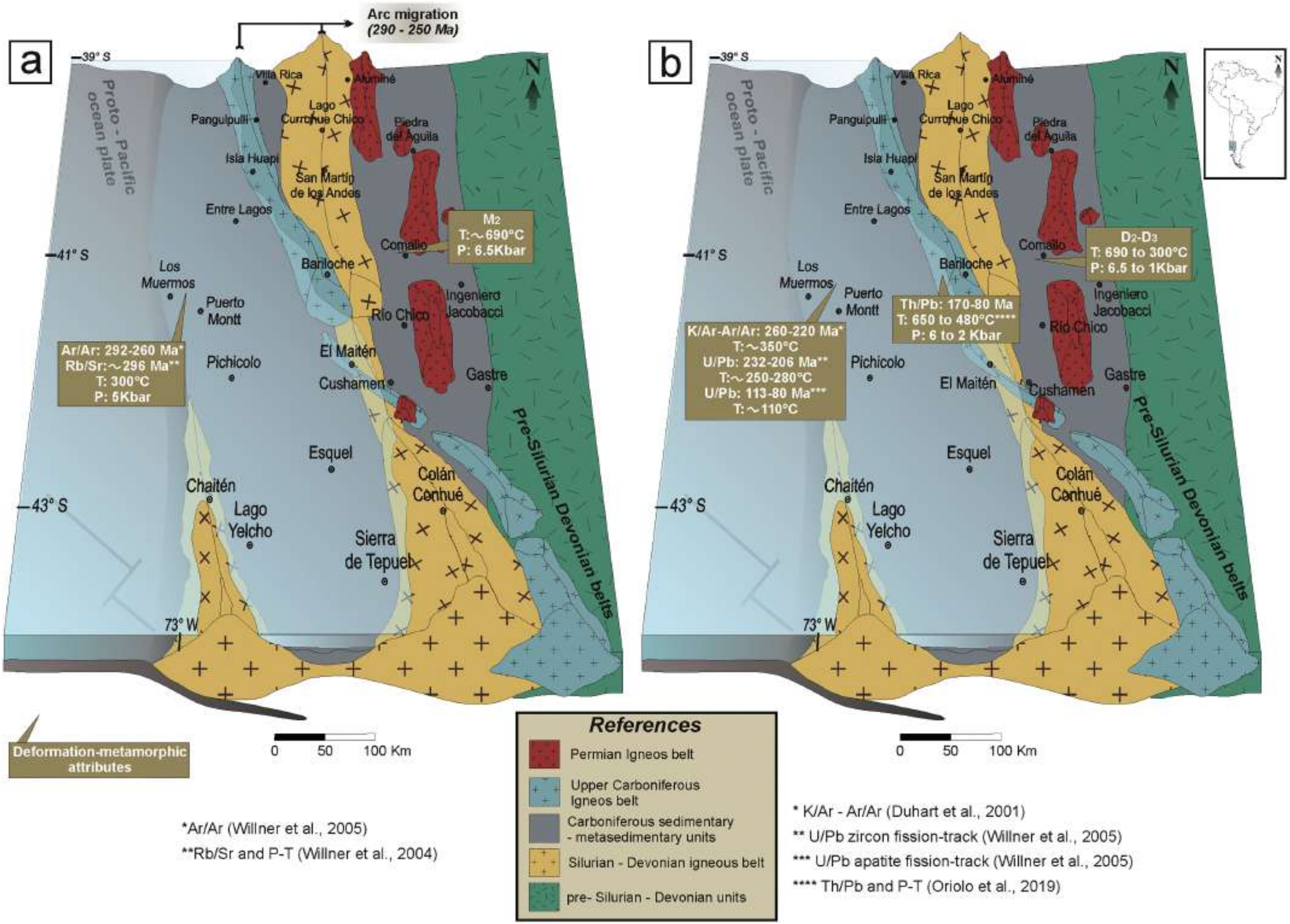

Arc migration
(290 - 250 Ma)
a
39° S
Proto - Pacific ocean plate
Villa Rica
Aluminé
Lago Curruhue Chico
Panguipulli
Piedra del Aguila
Isla Huapi
San Martín de los Andes
Entre Lagos
M2
T: ~690°C
P: 6.5Kbar
Comallo
41° S
Los Muermos
Bariloche
Puerto Montt
Ingeniero Jacobacci
Río Chico
Ar/Ar: 292-260 Ma*
Rb/Sr: ~296 Ma**
T: 300°C
P: 5Kbar
Pichicolo
El Maitén
Cushamen
Gastre
Pre-Silurian Devonian belts
Esquel
Chaitén
Colán Conhué
43° S
Lago Yelcho
Sierra de Tepuel
73° W
Deformation-metamorphic attributes
0 50 100 Km
*Ar/Ar (Willner et al., 2005)
**Rb/Sr and P-T (Willner et al., 2004)
b
39° S
D2-D3
T: 690 to 300°C
P: 6.5 to 1Kbar
Th/Pb: 170-80 Ma
T: 650 to 480°C****
P: 6 to 2 Kbar
K/Ar-Ar/Ar: 260-220 Ma*
T: ~350°C
U/Pb: 232-206 Ma**
T: ~250-280°C
U/Pb: 113-80 Ma***
T: ~110°C
References
Permian Igneos belt
Upper Carboniferous Igneos belt
Carboniferous sedimentary - metasedimentary units
Silurian - Devonian igneous belt
pre- Silurian - Devonian units
* K/Ar - Ar/Ar (Duhart et al., 2001)
** U/Pb zircon fission-track (Willner et al., 2005)
*** U/Pb apatite fission-track (Willner et al., 2005)
**** Th/Pb and P-T (Oriolo et al., 2019)

Figure 13

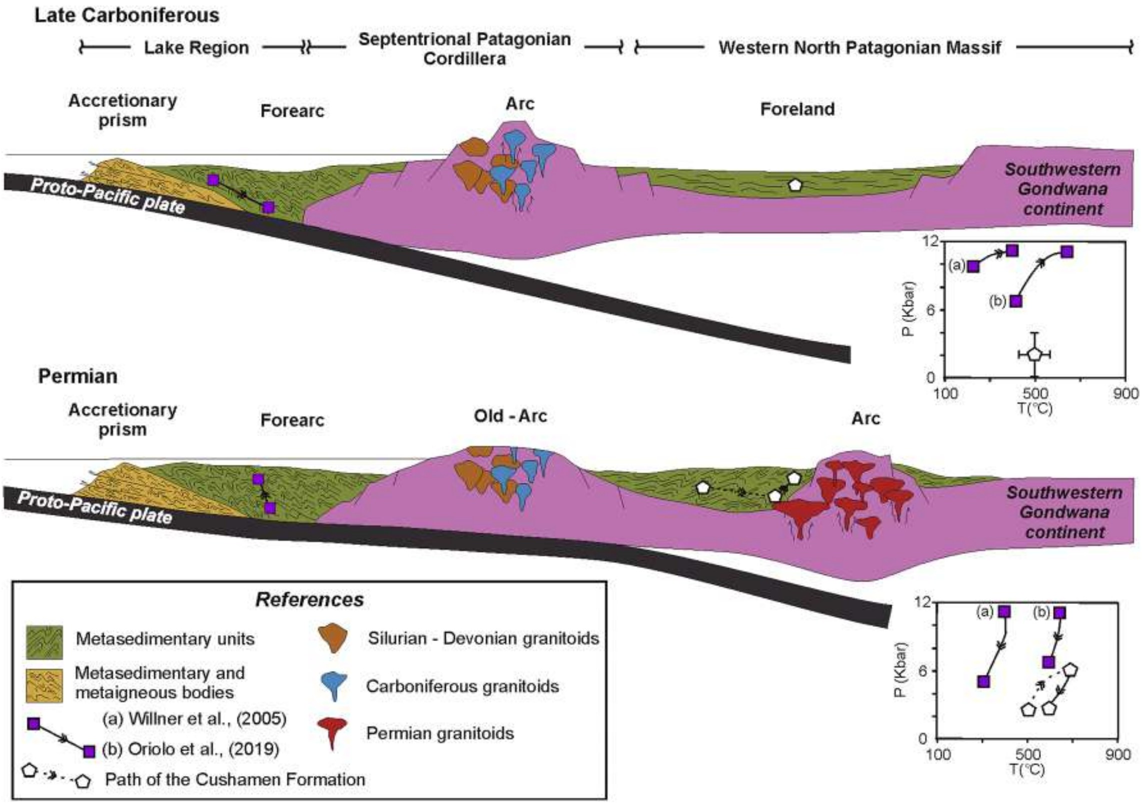
Late Carboniferous
Lake Region
Septentrional Patagonian Cordillera
Western North Patagonian Massif
Accretionary prism
Forearc
Arc
Foreland
Proto-Pacific plate
Southwestern Gondwana continent
(a)
(b)
P (Kbar)
T(°C)
12
6
0
100
500
900
Permian
Accretionary prism
Forearc
Old - Arc
Arc
Proto-Pacific plate
Southwestern Gondwana continent
(a)
(b)
P (Kbar)
T(°C)
12
6
0
100
500
900
References
Metasedimentary units
Metasedimentary and metaigneous bodies
(a) Willner et al., (2005)
(b) Oriolo et al., (2019)
Path of the Cushamen Formation
Silurian - Devonian granitoids
Carboniferous granitoids
Permian granitoids

Figure 14